Title

Structural Evolution of Pt Nanoclusters Driven by CO Reactant Pressure and Catalyst Temperature.

Journal

Journal of the American Chemical Society

ISSN

0002-7863

Authors

Tao, Franklin
Jiang, David
Nguyen, Luan
et al.

Publication Date

2026-06-01

DOI

10.1021/jacs.6c02758

Structural Evolution of Pt Nanoclusters Driven by CO Reactant Pressure and Catalyst Temperature

Franklin Tao,[†‡a]* David Jiang,[a¶] Luan Nguyen,[‡] Philippe Sautet[¶&]*

[†] Department of Materials Science and Engineering, University of California, Berkeley, California, 94706 USA
[‡] Department of Chemical and Petroleum Engineering, University of Kansas, Lawrence, Kansas, 66049 USA
[¶] Department of Chemical and Biomolecular Engineering, University of California, Los Angeles, Los Angeles, California 90095, USA
[&]Department of Chemistry and Biochemistry, University of California, Los Angeles, Los Angeles, California 90095, USA

ABSTRACT

The atomic-scale structure of a metal catalyst surface controls its catalytic performance. Through a combination of High-pressure Scanning Tunneling Microscopy (HP-STM), Ambient Pressure X-ray Photoelectron Spectroscopy (AP-XPS) and machine learning-accelerated computational studies we uncovered that Pt nanoclusters, formed by restructuring of hex-Pt(100) under reaction conditions involving CO, experience major structural evolution when exposed to increasing CO pressure in the range of 2×10^{-8}–750 Torr. Atom-resolved images and simulations demonstrate that CO binds strongly on these nanoclusters, leading to a CO coverage of one molecule per Pt atom while the lateral CO-CO repulsion is released by tilting CO molecules outward at the nanocluster edge. Metal nanoclusters break down along as CO pressure is increased from 2×10^{-8} to 1 Torr with the average size decreasing from 3.2±1.5 nm to 2.3±1.0 nm, consistent with Pt $4f_{7/2}$ photoemission feature evolution observed with AP-XPS. In contrast, in the pressure range of 1-750 Torr at 25ºC, HP-STM observed a decrease of nanocluster density by 4-5 times, consistent with a growth of the average nanocluster size from 2.3±1.0 nm in 1 Torr CO to 4.6±1.8 nm in 750 Torr. This uncovers a reactant pressure-driven coalescence of nanoclusters even at room temperature. Nanoclusters formed at 25ºC in 750 Torr CO require annealing to 100-130ºC to reach equilibrium size,

indicating kinetic control of nanocluster growth at low preparation temperatures. Our neural network potential (NNP) coupled with basin hoping (BH) simulations determined the optimal CO coverage and configuration at various CO pressures and showed, in agreement with experiments, an optimum nanocluster size resulting from a competition between the size-dependent energy cost of nanocluster formation and the energy gain through CO adsorption. The formation of Pt nanoclusters, followed by their breakdown with increasing CO pressure from 2×10^{-8} to 1 Torr and coalescence in CO pressure from 1 Torr to 750 Torr highlights the significance of imaging catalyst nanoparticle surfaces in gas phase at a specific reactant pressure towards establishing a direct structure-catalytic performance correlation.

[a] Authors contributed equally

*: To whom all correspondence should be addressed to: franklin.tao@Berkeley.edu (FT), sautet@ucla.edu (PS)

1. INTRODUCTION

Metal catalysts play a pivotal role in various fields of catalysis including thermal catalysis, electrocatalysis, and photocatalysis for chemical transformation and energy conversion. There are numerous reactions involving carbon monoxide (CO) as either a reactant or a product, including CO oxidation,[1–10] Fischer-Tropsch synthesis,[11] steam reforming of CH_4,[12–15] CO_2 reforming of CH_4,[16] partial oxidation of CH_4,[17] water-gas shift,[18] CH_3OH carbonylation,[19] hydroformylation,[20] and hydroaminoalkylation.[21] Most of these reactions are catalyzed by metal catalysts. However, there remains a lack of fundamental understanding of (1) the nature of metal sites active for reactions involving CO as a reactant or product and (2) how a perturbation such as variation of reactant or product pressure or elevation of catalysis temperature could restructure a metal surface.[12] Exploration of the surface structure of a metal catalyst is vital for understanding the catalytic reaction at a molecular level, as the metal surface structure dictates the binding of reactant molecules and the formation of intermediates on the metal catalyst. Platinum is particularly noteworthy among metal catalysts due to its activity in various reactions involved in sustainable chemical production, energy conversion, and clean fuel production.[22,23] Pt as a catalyst can activate the largest number of different reactions among all transition metals.[24] Thus, we selected Pt as a representative metal catalyst to explore atomic relocation of a catalyst surface driven by CO pressure and catalyst temperature.

Although ambient pressure X-ray photoelectron spectroscopy (AP-XPS) is effective for probing the surface chemistry of metal nanoparticles, it cannot resolve surface structures at the nanometer or atomic scale.[25–27] Extended X-ray fine structure (EXAFS) spectroscopy,[28] while informative about the coordination environment of the atoms of metal nanoparticles, struggles to distinguish surface structure from bulk. In contrast, high-pressure scanning tunneling microscopy (HP-STM) uniquely offers crucial information for identifying surface structure of a catalyst at nano and atomic scales by directly visualizing the surface of a catalyst, offering the highest surface sensitivity among all surface analytical techniques.[9,14,29–32] However, it can be challenging to gain atom-resolved images from a metal model catalyst surface at high pressure

conditions or perform scanning tunneling spectroscopy (STS) studies.[33–37] For this purpose, we designed and built a patented reactor-like HP-STM micropore, assembly, and system capable of imaging the surface structure of a model catalyst at elevated temperatures and pressures.[29,38]

Theoretical studies of surface phenomena in heterogeneous catalysis have advanced significantly with the development of density functional theory (DFT). However, computational studies investigating complex systems with larger unit cells and numerous adsorbates are limited due to the challenges associated with high computational cost and the multitude of possible adsorption configurations. Classical molecular dynamic simulations can handle large unit cells, but they rely on empirical force fields with a more limited accuracy. To address these challenges, we constructed a high dimensional neural network potential (HDNNP) for Pt and CO following the method developed by Behler and Parrinello.[39,40] This potential, trained on electronic energy data calculated with DFT using the Vienna *Ab initio* Simulation package (VASP)[41,42] with the Perdew–Burke–Ernzerhof (PBE) functional[43], accurately and efficiently describes adsorbate-adsorbate and adsorbate-surface interactions, allowing for efficient exploration of the vast potential energy surface (PES) of large unit cells with a high coverage of CO adsorbates. Additionally, a grand canonical basin-hopping (GCBH) algorithm was employed to capture the extensive number of possible CO coverages and adsorption sites, transforming the PES into local minima basins and transitioning between them via Monte-Carlo displacement trials.[44,45] This enabled us to explore the global minimum free energy as a function of number and configuration of CO adsorbates by fixing the chemical potential of CO, assuming that the surface exists in thermodynamic equilibrium with the CO gas at given conditions of temperature and pressure.[46–48]

In this article, a large number of Pt nanoclusters with an average size of 3.2±1.5 nm was prepared from hex-Pt(100) at room temperature and low CO pressure of 2×10^{-8} Torr. We aim to explore the dependence of nanocluster size on CO pressure and temperature and to determine the chemical and electronic factors that control the size. We tracked the structural evolution of these metal nanoclusters as a function of CO pressure up to 750 Torr at room temperature using HP-STM and AP-XPS and investigated

the thermodynamic stability of the formed Pt nanoclusters in CO at different conditions. It was found that the Pt nanoclusters initially formed at a low CO pressure of 2×10^{-8} Torr, break down into smaller nanoclusters with an average size of about 2.3±1.0 nm in CO at 1 Torr. In contrast, an increase of the CO pressure from 1 to 750 Torr results in an obvious coalescence of these nanoclusters into larger ones, even at room temperature. This coalescence creates metal clusters with an average size of 4.6±1.8 nm at 750 Torr, which is twice the size of the metal clusters at 1 Torr. This shows that Torr pressure of CO gas can drive significant relocation of metal atoms of nanoclusters. The temperature-dependent structural evolution in the range of 25-130^{o}C suggests that the structure of nanoclusters prepared at room temperature or lower is kinetically limited. The finding and insights gained through the synergistic efforts of in-situ experimental exploration of nanocluster structure and machine learning-assisted computational studies underscore the significance of exploring metal catalyst surface structure at specific reactant pressures and catalyst temperatures.

2. EXPERIMENTAL AND COMPUTATIONAL

2.1 Preparation of Pt nanocluster model catalyst

A Pt(100) single crystal (99.999% purity) was purchased from MaTeck GmbH (Germany). The surface was cleaned by repeated cycles of Ar^{+} sputtering (2×10^{-7} Torr Ar, 30 min), annealing at 850^{o}C in UHV, and subsequent annealing in 5×10^{-9} Torr O_2 to remove residual contaminants such as carbides, sulfides, and nitrides. Surface cleanliness was verified after each cycle using Auger electron spectroscopy (AES). After cleaning, the crystal was annealed at 900–950^{o}C for 5 min in UHV and slowly cooled to room temperature to form the hex-reconstructed Pt(100) surface. Formation of hex-Pt(100) was confirmed by STM imaging in UHV. Introduction of 2×10^{-8} Torr CO onto the hex-Pt(100) surface led to the formation of a Pt nanocluster model catalyst. The structural response of these nanoclusters to variations in CO pressure and temperature was investigated using high-pressure scanning tunneling microscopy (HP-STM) and

ambient-pressure X-ray photoelectron spectroscopy (AP-XPS) at synchrotron facilities at NSLS-II at Brookhaven Nation Lab.

2.2 Operando studies of metal nanoclusters in CO at different pressures and temperatures

Nanocluster structures were examined over a wide CO pressure range (2×10^{-8} to 750 Torr) and temperatures between 25 and 130ºC using an HP-STM system. The design and performance of this instrument have been reported previously. Briefly, the system consists of a sample preparation chamber equipped with heating/cooling capabilities and AES-LEED for surface characterization and a dedicated STM chamber. The STM chamber was designed to operate both under UHV conditions (base pressure $\sim1\times10^{-10}$ Torr) and in reactant gas up to atmospheric pressure. It comprises of an STM room and an independently sealed reaction cell. In UHV mode, the sample in the STM room is exposed to UHV for imaging. For gas-phase measurements, the reaction cell holding a model catalyst is sealed by a removable door and filled with reactant gas at a controlled pressure while maintaining STM imaging capability. The sample temperature can be controlled during experiments, enabling direct visualization of surface structures under a specific gas pressure and elevated temperature. This design allows atomic-scale imaging of Pt surfaces in both UHV and gas-phase environments over a pressure range spanning from 10^{-9} Torr to bar pressure. Images of the catalyst surface were taken in a constant current mode at a bias of 0.3 V and a current of 0.5 nA. Surface chemistry of the nanocluster model catalyst in UHV and CO at 10^{-8}-1 Torr was studied with the ambient pressure X-ray photoelectron spectrometer (AP-XPS) system at NSLS-II at Brookhaven National Lab. The details on data collection and measurement in HP-STM and AP-XPS studies can be found in Section 1 of Supporting Information.

We would like to note that, although comparison of nanocluster density between experiment and theory is rather direct, the comparison of nanocluster size should be performed with caution. First, the experimental mean diameters were reported based on the longest measurement of their dimensions. Calculated models are square. Rectangular models have been shown to provide similar energy compared to square models and would obviously provide a larger maximum size. Second, STM tends to overestimate

the size of imaged objects because the local density of state of the adsorbed CO due to fan-out effect at the tip apex position can extend further laterally. In addition, the tip apex has a finite size and tip convolution effects lead to further lateral broadening of the observed features.

2.3 Computational methods and machine learning integration

Density functional theory (DFT) calculations were performed using the Vienna *Ab initio* Simulation Package (VASP) with the PBE functional within the generalized gradient approximation. Slab models consisted of six Pt layers separated by a 15 Å vacuum region, with the bottom four layers fixed and the top layers relaxed. Brillouin zones were sampled using a 4×4×1 *k*-point mesh, and electronic occupations were treated using a second-order Methfessel–Paxton smearing of 0.2 eV. A previously developed correction scheme was applied to compute CO adsorption energies under varying pressure conditions.[48]

Gibbs free energies for gas-phase and adsorbed CO were obtained by combining DFT energies with zero-point energy and entropy corrections. Vibrational frequency calculations were used to determine ZPE and entropy contributions for adsorbed CO, while translational and rotational contributions were included for gas-phase CO. The potential energy surface was explored using the grand-canonical basin-hopping (GCBH) method, which simultaneously optimizes surface structures and CO coverage. Mutations included displacement of surface and cluster Pt atoms, variation of CO coverage, and rearrangement of adsorbed CO. Searches were terminated once high CO coverage was reached and no new structures were identified over 100 consecutive steps. To accelerate energy evaluations, a neural network potential (NNP) was developed using the n2p2 package. The training set comprised 5400 DFT-calculated structures, including flat and stepped Pt surfaces and small Pt clusters with varying CO coverages. The NN achieved root-mean-square errors below 0.6 meV/atom for training, validation, and test sets, demonstrating accuracy comparable to DFT for both small and larger Pt cluster configurations. More details can be found in Supporting Information.

3. RESULTS AND DISCUSSION

3.1 Hex-Pt(100) surface structure

A bare hex-Pt(100) was prepared in ultrahigh vacuum environment (UHV) with a base pressure of 1×10^{-10} Torr by following a standard literature protocol.[49] For the well-prepared bare hex-Pt(100), the topmost atomic layer does not show the square array of a 1×1-Pt(100) but instead adopts a two-dimensional hexagonal pattern resembling the (111) termination of a perfect Pt(111), while all other atomic layers under the topmost (111) layer retain the (100) pattern (see details in SI Figure S1).[50–57] (100) and hex are the abbreviations of 1×1-Pt(100) and hex-Pt(100) used in this article, respectively. The atomic density of the topmost atomic layer of the hex-Pt(100) is 125% of that of the atomic layers in the subsurface.[50,55,56] The hex-Pt(100) was modelled using a 5×5 supercell. In the lateral direction, *six* staggered atomic rows of the topmost atomic layer of hex-Pt(100), packed in pseudo (111) lattice are placed on top of *five* atomic rows in the subsurface layer (Figure S1and S2), corresponding to an atomic density increase of 120%. In our calculations, the hex-Pt(100) structure is more stable than the 1×1-Pt(100) by 0.035 eV/Å^2. This energetic stabilization for the denser hexagonal layer stems from an increase of Pt coordination in the surface layer to 9 neighbors in contrast to 8 at the 1×1-(100) surface.

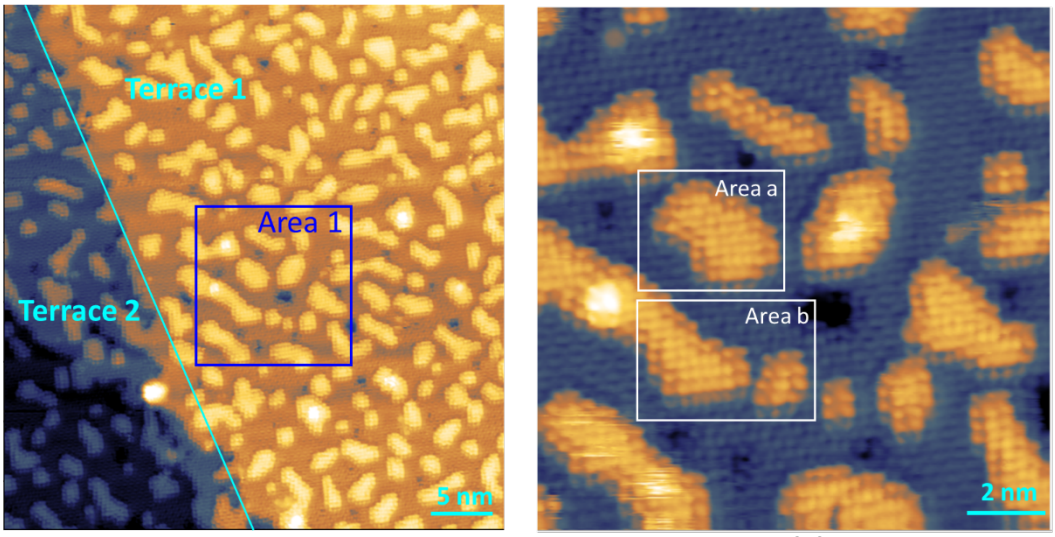

Figure 1. Atom-resolved STM image showing the formation of clusters on the Pt(100) surface in a CO pressure of 2×10^{-8} Torr at 25°C. The image was collected in constant current mode with our homemade HP-STM. (a) 42 nm×42 nm image showing two terraces. (b) Enlargement of area 1 (13 nm×13 nm) marked in (a); The color scale was tuned for visualizing the terrace region between nanoclusters.

3.2 Formation of Pt nanoclusters model metal catalyst

The clean hex-Pt(100) surface was exposed to CO at 25ºC under a pressure of 2×10^{-8} Torr and atom-resolved images were acquired under these conditions using HP-STM. The surface structure dramatically changed and massive nanoclusters, shown in yellow, were formed (Figure 1). This representative image (Figure 1a) has a size of 42 nm×42 nm and consists of two terraces, while an enlargement of Area 1 marked in Figure 1a is given in Figure 1b. The size distribution of these nanoclusters is 3.2±1.5 nm based on statistical accounting of STM images (entry 1 in Table 1). These nanoclusters exhibit different shapes from globular to markedly elongated. They are randomly dispersed on the base layer. Pt atoms of the base layer come from the topmost atomic layer of the original hex-Pt(100). Line-profile analysis (Supplementary Figure S4) shows that these nanoclusters are mostly one atomic Pt layer high. The base layer is shown in dark yellow on terrace 1 in Figure 1a. The color scale of Figure 1b was tuned for visualizing atomic packing of the base layer, now shown in blue tone. Although Figure 1a is a high-resolution image, the atomic arrangement of these nanoclusters and the region between the clusters cannot be readily identified due to the large size of the image. In Figure 1b enlargement, both the clusters (yellow) and the regions of the base layer between nanoclusters (blue) are imaged with atomic resolution. Each bright ball is mainly contributed from a CO molecule instead of its underlying Pt atom since CO is much closer to the STM tip than the Pt atom. From the literature, the base layer supporting these nanoclusters is a Pt(100) atomic layer where Pt atoms pack into a 2-D square lattice with a Pt-Pt separation of 2.79 Å.[49,58–60] Notably, these bumps between nanoclusters in Figure 1b represent CO molecules adsorbed on the base layer. The arrangement of these bumps between nanoclusters suggests that CO molecules adsorbed on the base layer do not pack into a (100) lattice.

Table 1. List of density and average size of nanoclusters at different pressures and temperatures

Entry	Pressure (Torr)	Temperature (ºC)	Density (nm^{-2})	Average Size (nm)
1	2×10^{-8}	25	0.103±0.006	3.2±1.5
2	2×10^{-6}	25	0.125±0.007	2.8±0.9

3	1	25	0.158±0.008	2.3±1.0
4	50	25	0.087±0.007	3.0±1.0
5	100	25	0.061±0.006	3.2±1.1
6	750	25	0.048±0.005	4.6±1.8
7	750	100	0.028±0.003	7.5±2.5
8	750	130	0.023±0.002	7.8±2.6
9	750	25	0.023±0.002	8.0±2.8

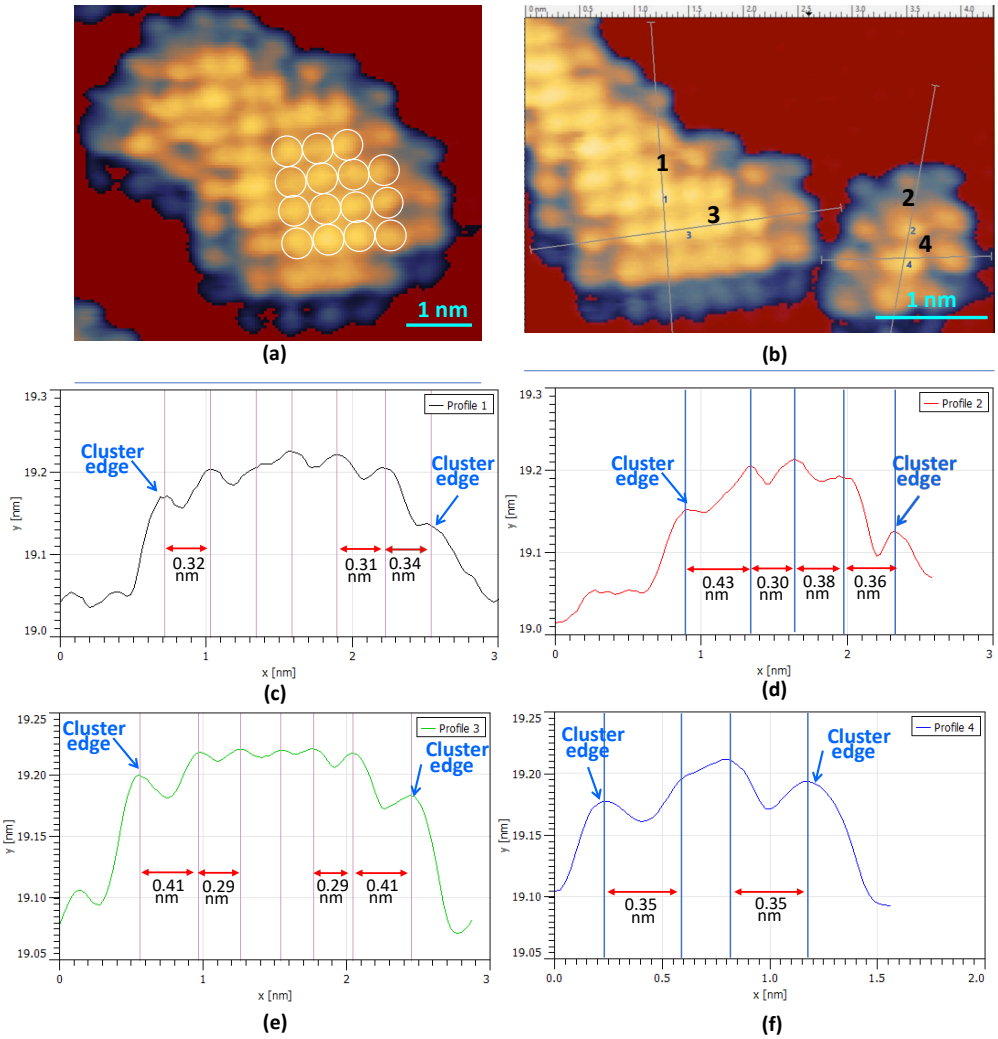

Figure 2. Atom-resolved HP-STM images and line profile analysis of nanoclusters formed by restructuring hex-Pt(100) in CO at 2×10^{-8} Torr at 25°C. (a) Atom-resolved image (3.5 nm×3.1 nm) of the nanocluster Area *a* in Figure 1b. (b) Atom-resolved image (4.2 nm×3.2 nm) of the nanoclusters in Area *b* in Figure 1b. (c-f) STM topographic profiles along lines 1, 2, 3, and 4 in (b). The distances between two adjacent bumps are marked in these line profiles.

One feature of the nanocluster model metal catalyst in Figures 1b, 2a, and 2b is that the atoms at the edges of nanoclusters exhibit a lower contrast (appearing as blue in Figure 2a and 2b) than the inner atoms of these nanoclusters (appearing as bright yellow). The line-profile analyses in Figure 2c-2f confirm

that the heights of CO molecules adsorbed on Pt atoms at the nanocluster edges marked as "edge CO" in Figure 2c-2f are lower than CO molecules on inner Pt atoms of the nanoclusters. The lower contrast is due to a fan-out effect of these CO molecules for minimizing the intermolecular repulsion between the CO molecules on edge-Pt atoms and those on inner-Pt atoms. Figure 2 is evidence of this molecular fan-out effect being observed for the first time.

At room temperature and CO gas of 2×10^{-8} Torr, the average size of these formed Pt nanoclusters is 3.2±1.5 nm. It corresponds to a nanocluster density of 0.103 cluster/nm^2. The formed Pt nanoclusters in Figure 1a were used as a model of metal nanoparticle catalysts to explore how these catalysts respond to the perturbation of reactant gas pressure and catalyst temperature.

In the following subsections, nanocluster density was used as the primary metric to evaluate nanocluster breakup or coalescence. Nanocluster density was defined as the number of nanoclusters counted within a specified surface area. This approach was adopted because counting nanoclusters in a defined region (e.g., 42 nm×42 nm) provides robust statistics, whereas direct size measurements are less reliable due to the irregular, bent, or U-shaped morphologies of many nanoclusters. In this system, nanocluster density is directly related to nanocluster size because the total number of Pt atoms contained in all nanoclusters is fixed at 25% of a Pt(100) atomic layer, resulting from the release of the hex reconstruction. Nanocluster density was calculated as N/M (nm^{-2}), where N is the number of nanoclusters and M is the imaged area. For each pressure or temperature condition, nanocluster densities were determined from multiple large-area STM images acquired under identical conditions. Average nanocluster sizes and size distributions were also measured and are provided for comparison to verify consistency with trends observed in the density analysis.

3.3 Thermodynamics of formation of Pt nanoclusters of different sizes in CO at 2×10^{-8} Torr

By using our trained NNP as described in Section 2.3, the structure of Pt nanoclusters supported on 1×1-Pt(100) under a CO pressure of 2×10^{-8} Torr was modeled. We considered square one-atomic-layer

nanoclusters ranging in size from the smallest 3×3 nanocluster consisting of 9 atoms, to the largest 13×13 nanocluster of 169 atoms. Rectangular clusters of size 4×9 were considered as well (Figure S6). We assume that the topmost hex-Pt(100) layer forms into a 1×1-Pt(100) atomic layer with nanoclusters above that layer. The ratio of nanoclusters atoms to the 1×1-Pt(100) base layer atoms is fixed at 0.25. Therefore, the n×n nanocluster is placed on a 2n×2n Pt(100) unit cell (containing $4n^2$ Pt atoms in its surface layer). Such a system (nanocluster and supporting terrace) will be called a n×n system (see Figure 3 for a representation of a 3×3 nanocluster on a 6×6 unit cell). Based on this model, the number of accessible Pt atoms at the terrace region between these nanoclusters is $3n^2$ ($=4n^2-n^2$) which is about 3 times the number of Pt atoms (n^2) of the (n×n) nanocluster (Figure 3a). Here, we refer to the accessible surface of the base layer between (n×n) nanoclusters as the terrace. For example, the terrace region between the nanoclusters of the 3×3 system is marked in yellow in Figure 3a.

In the absence of CO adsorbates, the hex-Pt(100) is the most stable system with the lowest surface energy of 0.20 eV/Å^2 (blue dashed line in Figure 3d and Table S1) compared to 0.23 eV/Å^2 for the bare 1×1-Pt(100). The black dots in Figure 3d mark the surface energies of bare (n×n) systems (n=3-8). These bare (n×n) systems (n=3-8) are obviously less stable than the bare hex-Pt(100) (blue dashed line in Figure 3d) and the bare 1×1-Pt(100) (red dashed line in Figure 3d), indicating that nanoclusters are not stable in the absence of CO. A clear and natural trend found in Figure 3d is that the surface energy of a bare n×n system decreases along with the increase of size since the fraction of low coordination Pt atom decreases.

The CO coverage and configuration were globally optimized by extensive GCBH simulations. These simulations were performed with the surface being in thermodynamic equilibrium with gas phase CO as defined by temperature and pressure parameters matching those of the experiment. Based on what is seen in the STM images in Figures 1 and 2, neither a (sub)monolayer coverage nor a multilayer of CO adsorbed on a (n×n) system is considered at the temperature of 25ºC. The structure with the most stable equilibrium coverage and configuration is selected out of the total ensemble found via GCBH simulations. The total energy, E_{NNP}, for a n×n system was predicted and used to calculate the formation energy which

was normalized by surface area to yield surface energy in eV/Å^2. The formation energy (FE) is found using the predicted energy from the NNP through the formulae: $FE = E_{NNP} - n \times \mu_{Pt} - m \times \mu_{CO}$ where n, m, μ_{Pt}, and μ_{CO} represent the number of Pt atoms, the number of adsorbed CO molecules, the chemical potential of bulk Pt, and the chemical potential of gas-phase CO at 25ºC at the considered CO pressure, respectively. FE includes both the temperature and CO pressure dependence. μ_{CO} was calculated with DFT using the equation: $\mu_{CO} = E_{CO} + \left(ZPE^{gas} + C_p^{gas} - TS^{gas}\right) - (ZPE^{ads} + C_p^{ads} - TS^{ads})$.

When CO molecules are adsorbed on Pt surfaces at 25ºC in 2×10^{-8} Torr CO in Figure 3c, the stability order completely changes (Figure 3c versus 3d). The hex-Pt(100) is slightly stabilized by CO adsorption with a surface energy of 0.17 eV/Å^2 (blue dashed line in Figure 3c), which is lower than the 0.20 eV/Å^2 for the bare hex-Pt(100) (blue dashed line in Figure 3d). While hex-Pt(100) is the most stable termination in the absence of CO, it becomes the least stable system in the presence of CO in Figure 3c. Notably, these Pt nanocluster systems are all markedly stabilized by 0.2-0.3 eV/Å^2 upon CO adsorption (black dots in Figure 3c compared to Figure 3d) and become the most stable structures. Finally, the 1×1-Pt(100) is significantly stabilized by CO, becoming more stable than the hex termination, but less stable than the (n×n) nanoclusters in Figure 3c. Therefore, the transformation of hex-Pt(100) into (n×n) nanoclusters of Pt in 2×10^{-8} Torr CO is calculated to be thermodynamically favorable. The calculated optimal size for the 6×6 nanocluster matches the experimentally measured cluster density of 0.102 nm^{-2}, marked with a vertical black dashed line in Figure 3c. However, the favorable thermodynamics in forming any of these (n×n) systems (n=3-8) from hex-Pt(100) and the small energy difference among these (n×n) systems (n=3-8) in Figure 3c justify why Pt nanoclusters with different sizes can coexist in 2×10^{-8} Torr CO in the experimentally observed image (Figure 1).

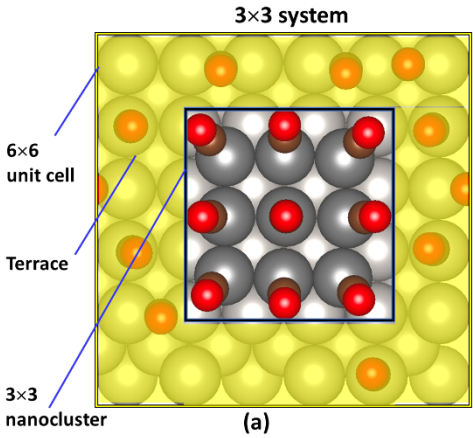
3×3 system
6×6
unit cell
Terrace
3×3
nanocluster

(a)

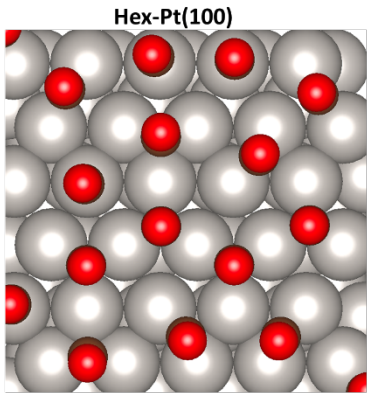
Hex-Pt(100)

(b)

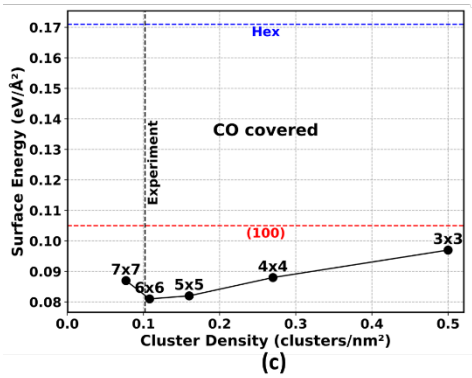
Hex
CO covered
Experiment
(100)
7x7
6x6
5x5
4x4
3x3
Surface Energy (eV/Å²)
Cluster Density (clusters/nm²)

(c)

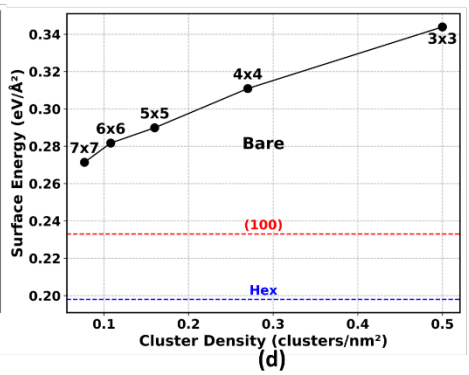
Bare
(100)
Hex
7x7
6x6
5x5
4x4
3x3
Surface Energy (eV/Å²)
Cluster Density (clusters/nm²)

(d)

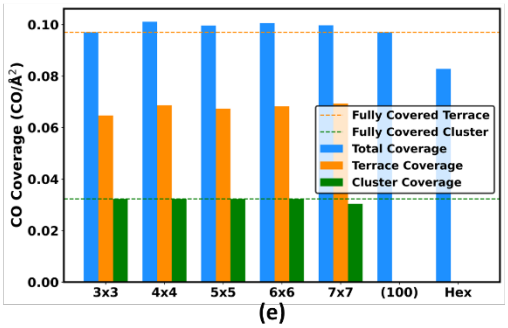
Fully Covered Terrace
Fully Covered Cluster
Total Coverage
Terrace Coverage
Cluster Coverage
CO Coverage (CO/Å²)
3x3
4x4
5x5
6x6
7x7
(100)
Hex

(e)

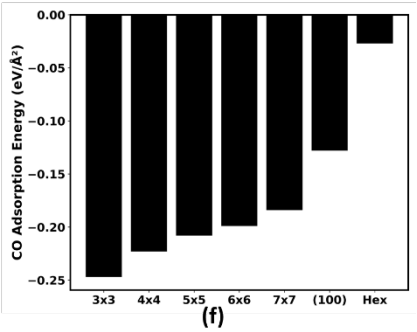
CO Adsorption Energy (eV/Å²)
3x3
4x4
5x5
6x6
7x7
(100)
Hex

(f)

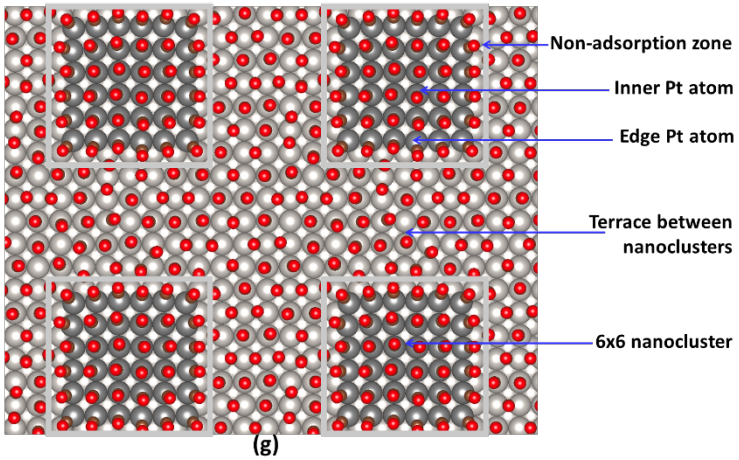
Non-adsorption zone
Inner Pt atom
Edge Pt atom
Terrace between
nanoclusters
6x6 nanocluster

(g)

Figure 3. Calculated surface energies and CO coverages on (n×n) systems consisting of a n×n square Pt nanocluster on a 2n×2n unit cell of the Pt(100) surface for n=3-8. (a) Structure example for the (3×3) Pt cluster on the 6×6 unit cell (3×3 system) with the optimal CO configuration at a pressure of 2×10^{-8} Torr. (b) Structure example for the (111) lattice of the topmost atomic layer of hex-Pt(100) with the optimal CO configuration at a pressure of 2×10^{-8} Torr. (c) Surface energies calculated with NNP for the (n×n) systems in a CO pressure of 2×10^{-8} Torr plotted as a function of the cluster density (number of nanoclusters per nm^2). For each system, the optimal CO coverage and arrangement is obtained by grand canonical basin hopping (GCBH) simulations. Surface energies of CO covered 1×1-Pt(100) and hex-Pt(100) are indicated by the horizontal red and blue dashed lines, respectively, while the cluster density for the considered CO pressure measured by HP-STM at 25°C is given by a vertical black dashed line. (d) Surface energies calculated with NNP for the bare (n×n) systems plotted as a function of the cluster density along with bare Pt(100) and hex-Pt(100). (e) Calculated optimal CO coverage ($CO/Å^2$) on the (n×n) systems (blue bars) decomposed in contribution of CO adsorbed on the cluster part (green bars) and on the terrace in between cluster (orange bars). The optimal CO coverages on 1×1-Pt(100) and Pt(100)-hex surfaces are also given. For 1×1-Pt(100) and hex-Pt(100), total coverage and terrace coverage are identical as no cluster is present on either system. (f) Surface area normalized adsorption energies of CO under CO pressure of 2×10^{-8} Torr, for (n×n) systems, 1×1-Pt(100) and hex-Pt(100). (g) Optimized surface structure for the (6×6) Pt nanoclusters on the 12×12 unit cell of 1×1-Pt(100) (6×6 system) with optimal CO coverage and configurations at a pressure of 2×10^{-8} Torr. The non-adsorption zone on the terrace in the vicinity of the cluster is indicated by the green border.

3.4 Size-dependent thermodynamics of Pt nanoclusters in CO

As shown in Figure 1, nanoclusters of different sizes coexist. The energetics and adsorbate structure for these nanoclusters are compared to 1×1-Pt(100) and the hex-Pt(100) in this subsection. The CO coverage in Figure 3e is defined as the ratio of the number of CO molecules adsorbed on the n×n system (nanocluster or terrace) to the surface area of that n×n system. Partial coverages are defined as the ratio of the number of CO molecules on the nanocluster/terrace to the total surface area of the n×n system and they sum to the total coverage. The calculated total CO coverage on the 1×1-Pt(100) without any clusters, 0.097 $CO/Å^2$ (blue bar marked with (100) in Figure 3e), corresponds to 0.75 CO per surface Pt atom. It is larger than that on the hex-Pt(100), 0.083 $CO/Å^2$. The higher CO coverage on 1×1-Pt(100) in 2×10^{-8} Torr CO is one reason why 1×1-Pt(100) has a lower surface energy than hex-Pt(100) in CO (Figure 3c). Another reason is that the adsorption energy of CO on a Pt atom of 1×1-Pt(100) is higher than that on a Pt atom of hex-Pt(100) because the surface Pt atom coordination, CN(Pt-Pt), is 8 for 1×1-Pt(100) but 9 for hex-Pt(100).

Computational studies found that the 6×6 nanocluster (Figure 3g), which is the most stable nanocluster among (n×n) nanoclusters (n=3-8), chemisorbs CO with a full coverage (100%). In other words,

each Pt atom of the 6×6 nanocluster chemisorbs one CO molecule through an on-top binding of CO as shown in Figure 4b and 4c.

Pt atoms of nanoclusters smaller than 6×6 also have a complete CO coverage, corresponding to 0.032 CO/Å^2 for the cluster coverage (green bars marked with 3×3, 4×4, 5×5, and 6×6 in Figure 3e) and incomplete coverage for the terrace (0.065-0.072 CO/Å^2, orange bars in Figure 3e). For larger clusters such as 7×7 and 8×8, the CO coverage on the cluster is calculated to be not complete with three CO less than Pt cluster atoms (Figure S10e) for 7×7 and five CO less than Pt cluster atoms for 8×8 (Figure S10f). The total CO coverage on these n×n systems (n=3-8) is 0.1-0.102 CO/Å^2, only barely higher than that on the pristine (100), 0.097 CO/Å^2 (green bars in Figure 3e). This indicates that the local CO coverage on the exposed terrace region between the nanoclusters (estimated to 0.084-0.092 CO/Å^2) is lower than the CO coverage on the (100), 0.097 CO/Å^2. This is mainly because terrace Pt atoms at the peripheral region of a n×n nanocluster are blocked for CO adsorption as CO molecules on the edge of the Pt nanocluster fan out to release intermolecular repulsion. Figure 4c shows the blocking effect of the fan-out CO on the terrace Pt atoms underneath. The fan-out phenomenon prevents the terrace Pt along the periphery of the nanocluster from adsorbing CO molecules, creating a *non-adsorption zone* around the nanocluster. This non-adsorption zone at the interface of the nanocluster and the terrace is marked with a green border in Figure 3g.

The primary reason why nanocluster surfaces, although less stable than 1×1-Pt(100) in vacuum, become the most stable terminations under CO pressure is the stronger adsorption of CO at the edge and corner atoms of the nanoclusters which have a Pt-Pt coordination of 6 and 5, respectively. Although these nanoclusters only occupy 1/4 area of the surface, it results in a marked increase in the absolute value of the overall adsorption free energy of CO, which makes the n×n nanocluster systems more negative, and hence stable, compared to the 1×1-Pt(100) surface (Figure 3f). This effect is maximal for very small clusters (such as 3×3) since the fraction of atoms at edges and corners is higher for a smaller n×n nanocluster, resulting in a trend where a surface with the smallest clusters has the highest and thus least stable surface energy in UHV (1×10^{-10} Torr), but receives the strongest stabilization effect by CO adsorption at 2×10^{-8} Torr CO. The

CO stabilization effect decreases with the increase of nanocluster size since the influence of the edges and corners of the clusters becomes proportionally smaller. The adsorption energy of CO molecules on a nanocluster system approaches the value of the (100) surface with increasing cluster size (Figure 3f). Driven by two opposing trends, the surface energy of large nanoclusters covered with CO should converge towards the (100) value. As a result, an optimum exists at a medium cluster size for CO pressure of 2×10^{-8} Torr, that being the 6×6 cluster (Figure 3c).

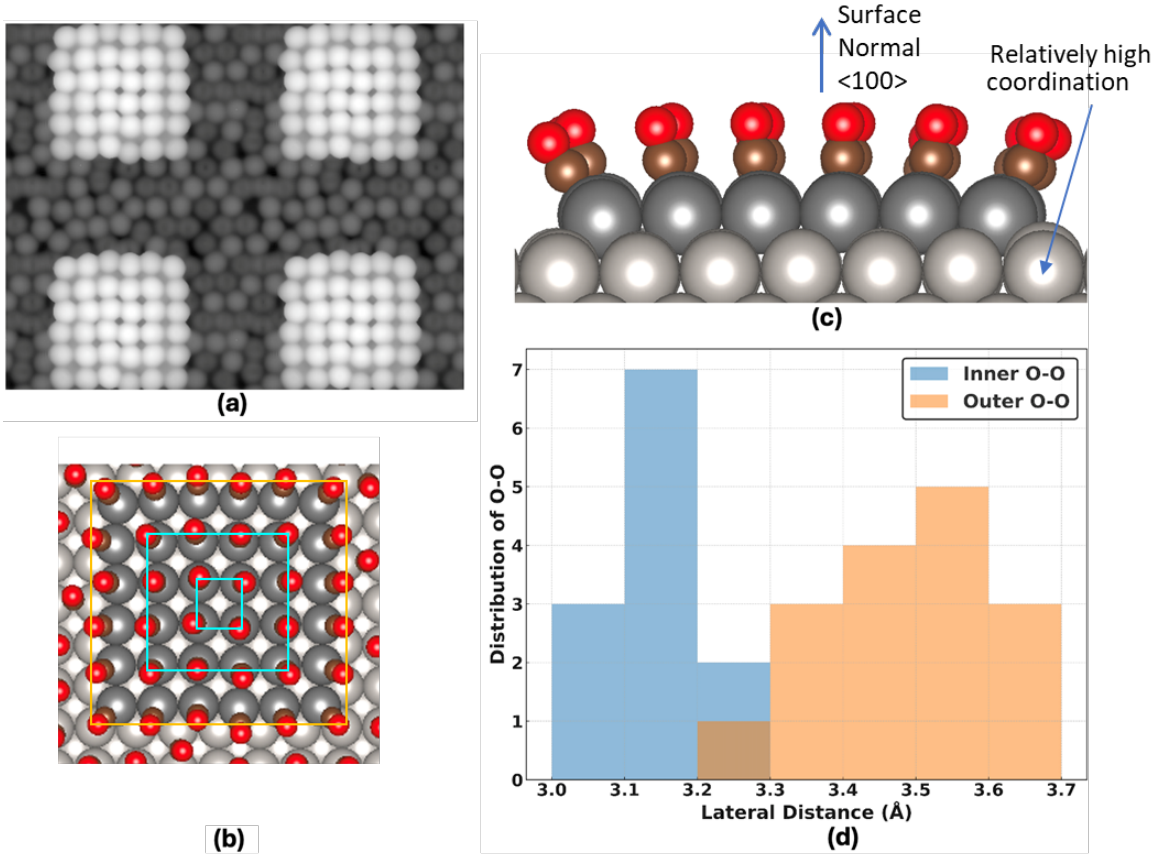

Figure 4. Simulated topographic STM image for the most stable structure of the (6×6) nanocluster at 25ºC in CO gas at pressure of 2×10^{-8} Torr and analyses of O-O distance of adsorbed CO molecules on the (6×6) cluster. (a) VASP simulated STM image. (b) Atomic structure of the (6×6) cluster seen from top view (O: red; C: brown; Cluster Pt: dark grey; Terrace Pt: light grey. (c) Side view of atomic structure, illustrating the tilt of CO molecules away from the cluster center. (d) Distribution of O-O lateral distances for CO molecules adsorbed on the (6×6) nanocluster with a color distinction between O-O separations involving edge CO molecules (outer O-O) or not (inner O-O).

3.5 Atomic scale structure of adsorbates on nanoclusters: proof of molecular fan-out effect along metal nanocluster edge

We found that the contrasts of CO on Pt atoms at the edge of nanoclusters in experimentally observed STM images (Figure 1b and Figure 2a and 2b) are clearly lower than for CO on the inner part of the nanocluster. For instance, the edge and inner parts of a nanocluster appear as blue and yellow, respectively in Figure 2a and 2b. These bright yellow bumps pack into a (100) lattice with an interatomic distance of 0.29-0.31 nm (Figure 2c and 2e). The bump-bump distances in the inner part of a nanocluster are only slightly larger than the interatomic distance of 0.279 nm between two adjacent Pt atoms in a standard (100) surface lattice of Pt. However, the distances between bumps near the edge of the clusters in Figure 2a and 2b are considerably larger than 0.279 nm. This can be seen in more detail from the line-profile analyses (Figure 2c, 2d, 2e, and 2f) conducted on the two nanoclusters in Figure 2b. In the direction of line 2 in Figure 2b, the distance between the edge bump and its adjacent inner bump is as large as 0.36 nm or even 0.43 nm (Figure 2d), which is most definitely larger than the 0.28-0.31 nm range of bump-bump distances in the inner part of the nanoclusters. Similarly, the relatively large separations between the edge bumps and their adjacent inner bumps are 0.32-0.34 nm in Figure 2c for line 1, 0.41 nm in Figure 2e for line 3, and 0.35 nm in Figure 2f for line 4. These “large” distances between the edge bumps and their adjacent inner bumps show that the CO molecules on the edge Pt atoms of the nanocluster fan out by tilting away from the CO molecules on the inner Pt atoms of the nanocluster. In addition, the CO molecules on the edge Pt atoms appear lower along the surface normal compared to a CO on the inner Pt atoms, as marked with “edge CO” in Figure 2c-2f. This effect is supported by our simulation (Figure 4c). The observed difference in image contrast in Figures 1b, 2a and 2b along with the measured line profiles in Figure 2c-2f is the first evidence of the fan-out effect of adsorbed molecules at the edge of a metal nanocluster while the fanning effect was hypothetically proposed in the first observation of surface restructuring of metal catalysts.[63]

Figure 4a shows the simulated STM image of (6×6) nanoclusters generated from NNP modeling at 2×10^{-8} Torr CO and 25ºC. The STM image results from the local density of states (LDOS) of the surface at the position of the lowest tip apex atom, which is dominated by the contribution of the O atoms of CO molecules adsorbed on Pt atoms because these O atoms are located at a much higher z position than the C and Pt atoms below. Since the contrast of each bump is mainly contributed from the O atom, the lateral distance between the bumps in the STM images reflects the separation between O atoms of adjacent CO molecules rather than the distance between two underlying Pt atoms. Figure S7a and S7b list the calculated Pt-Pt distances between Pt atoms of a 6×6 nanocluster on Pt(100) in UHV without any adsorbates and those of a 6×6 nanocluster with an adsorbed CO molecule on each Pt atom, respectively. There is no significant difference in Pt-Pt distance between bare (6×6) in Figure S7a and (6×6) with adsorbed CO molecules in Figure S7b. It further suggests that the contrasts of bumps in the simulated STM image in Figure 4a are attributed to the O atoms of adsorbed CO molecules instead of their underlying Pt atoms.

In the simulated STM image (Figure 4a), bumps are more separated near the periphery of the nanoclusters and their contrasts are lower, in very good agreement with experimentally observed STM images in Figure 2a and 2b because these CO molecules are tilted laterally away from their inner neighbors and their O atoms are physically lower than those of their neighbors along with the surface normal (Figure 4c). This tilting enables the minimization of the repulsion between CO molecules adsorbed on the edge Pt atoms and those on the inner Pt atoms, allowing the CO coverage on the nanoclusters to reach 1 ML.

To illustrate the various O-O separations between CO molecules adsorbed on a 6×6 nanocluster, we have classified the Pt atoms and their CO molecules in three categories in Figure 4b including the inner ring in the center of the 6×6 nanocluster, the second ring, and the outer ring along the periphery. In Figure 4b the blue squares mark the locations of O atoms of CO adsorbed on the inner ring and second ring and the orange square marks the outer ring. The distribution of the calculated O-O distances in Figure 4d clearly shows (1) the inner O-O separation between the inner ring and the second ring O atoms (blue bars in Figure 4d), 3.0-3.2 Å is slightly larger than the Pt-Pt separation (2.79 Å), and (2) the outer O-O separation between

the second ring and outer ring O atoms (orange bars in Figure 4d, 3.2-3.7 Å) is markedly larger than the Pt-Pt separation (2.79 Å). Thus, these O-O separations generated from computational studies further support the observed fan-out effect of CO molecules at the nanocluster edge.

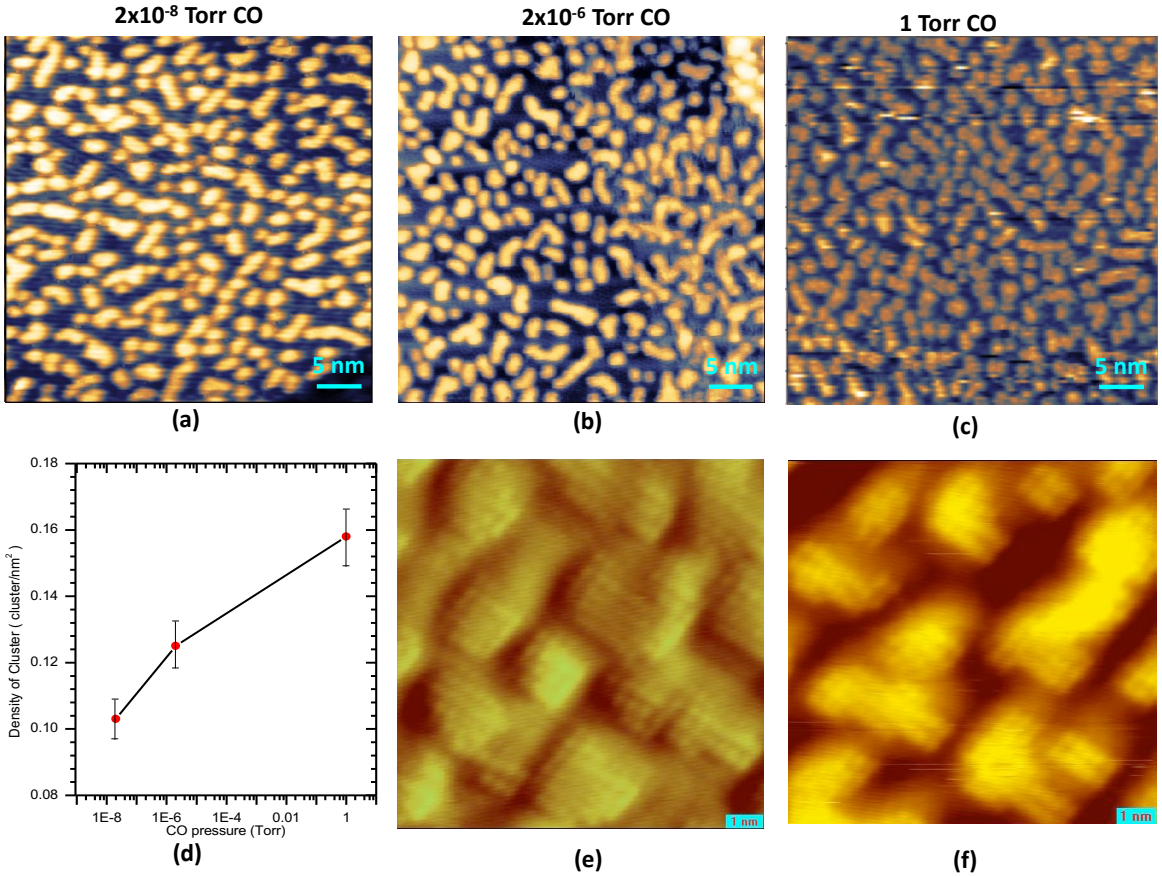

Figure 5. STM images of Pt nanoclusters at 25°C in CO gas at different pressure and measured density of Pt nanoclusters at different CO pressures. All images collected in gas phase at the marked pressure. (a) 2×10^{-8} Torr; Image size: 42 nm×42 nm. (b) 2×10^{-6} Torr; 42 nm×42 nm. (c) 1 Torr; 42 nm×42 nm. (d) Plot of density of nanoclusters as a function of CO pressure. (e) Atom-resolved image of nanoclusters in 2×10^{-6} Torr CO; 9.0 nm×9.0 nm. (f) Atom-resolved image of nanoclusters in 1 Torr CO; 9.0 nm×9.0 nm.

3.6 Coexistence of nanoclusters of varying shapes

As observed in Figure 1a, different shapes of nanoclusters with a size distribution of 3.2±1.5 nm are clearly observed. To check for the potential influence of nanocluster shape on thermodynamic stability, nanoclusters with the same number of Pt atoms but different shapes were simulated and their surface energies were calculated. For instance, the square 6×6 system in Figure 4b was compared with a rectangular

4×9 system in Figure S6. Both 6×6 and 4×9 nanoclusters have the same number of Pt atoms (36) and CO molecules (36) (Figure 4b and Figure S6). Computational studies found that they have very similar surface energies. This suggests little difference in stability between two nanoclusters of varying shapes but equal number of Pt atoms and adsorbed CO molecules. Thus, the nanocluster shapes play a minimal effect on the surface energy of nanoclusters decorated with CO, rationalizing the coexistence of nanoclusters with a wide range of irregular shapes at 25ºC in CO at 2×10^{-8} Torr (Figure 1a).

3.7 Slight breakdown of nanoclusters with the increase of CO pressure from 10^{-8} to 1 Torr

We explored the influence of an increased CO pressure, first in the range of 2×10^{-8}-1 Torr. Figure 5a-c presents representative HP-STM images collected at 25ºC from nanoclusters in the pressure range of 2×10^{-8} to 1 Torr. HP-STM is a unique tool to study the surface of hex-Pt(100) in CO pressures ranging from 1 Torr to 1000 Torr where most of AP-XPS systems cannot access this pressure range, although a very recent custom-designed AP-XPS system using hard-X-ray of high flux density to excite photoelectrons was reported to work at bar pressure range.[61] Statistical analysis of a large number of STM images collected at three different pressures reveals an increase in nanocluster density with increasing CO pressure as plotted in Figure 5d. It suggests that nanoclusters formed at 2×10^{-8} Torr break down, forming smaller nanoclusters. The average size of these nanoclusters, 3.2±1.5 nm in CO at

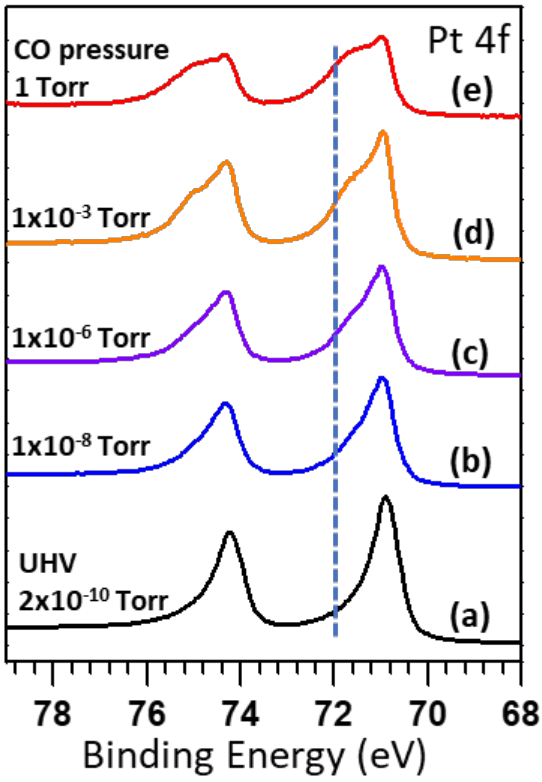

Figure 6. Pt 4f XPS spectra of (a) hex-Pt(100) at 25ºC in UHV and (b-e) Pt nanoclusters at 25ºC in CO at 1×10^{-8} Torr, 1×10^{-6} Torr, 1×10^{-3} Torr, and 1 Torr. The shoulders of Pt 4f7/2 are marked with the dashed line.

2×10^{-5} Torr CO, decreases to 2.3±1.0 nm in CO at 1 Torr. The decrease of average nanocluster size suggests that Pt nanoclusters at 1 Torr have a larger proportion of Pt atoms comprising the edges of nanoclusters than at 2×10^{-8} Torr. The increase of fraction of Pt atoms at nanocluster edges as CO pressure increases was supported by AP-XPS studies (Figure 6).

Figure 6 presents the Pt 4f spectra of surface Pt atoms at 25ºC in 2×10^{-8} Torr CO, 1×10^{-6} Torr CO, 1×10^{-3} Torr CO, and 1 Torr CO. An observable feature in these AP-XPS spectra is the appearance of the shoulders at about 71.9 eV on the high binding energy (BE) sides of the Pt $4f_{7/2}$ peaks marked with a dashed line. As shown in Figure 6d-e, the shoulder at about 71.9 eV becomes obvious at 1×10^{-3} Torr CO and especially at 1 Torr CO. According to literature,[14,62,63] a peak at 72.05 eV of Pt $4f_{7/2}$ for Pt(557) in 1 Torr CO was assigned to the highly undercoordinated Pt atoms at the edge of the formed triangular nanoclusters. Thus, the observed shoulders of Pt $4f_{7/2}$ at 71.9 eV in Figure 6b-e are contributed from the edge Pt atoms of these Pt nanoclusters formed in CO. The increase of the portion of the shoulder at 71.9 eV in these Pt $4f_{7/2}$ peaks along with the increase of CO pressure in Figure 6 shows that the atomic fraction of edge Pt atoms increases with CO pressure from 2×10^{-8} to 1 Torr. Thus, the AP-XPS finding confirmed the breakdown of nanoclusters along with increasing CO pressure observed in HP-STM (Figure 5a-d).

Figure 7a presents the calculated surface energies for nanoclusters of various sizes at CO pressure of 1 Torr. Surface energies for the bare nanoclusters can be seen in Figure 3d. By comparing Figure 7a with Figure 3c, one sees that all structures under elevated CO pressure are further stabilized compared to the low pressure condition, corresponding to a decrease of their surface energy, especially the 1×1-Pt(100) surface, which becomes close in stability to the nanocluster systems. In this range of pressure, the CO coverage is significantly increased on the 1×1-Pt(100). In contrast, the nanoclusters are already saturated (with 1 CO molecule per Pt atom) at low CO pressure (2×10^{-8} Torr) and hence the CO coverage can only increase on the terrace region in-between the clusters. At 1 Torr (Figure 7a) the most stable structure is a surface containing a nanocluster of size 5×5 instead of the 6×6 nanocluster seen at 2×10^{-8} Torr (Figure 3c).

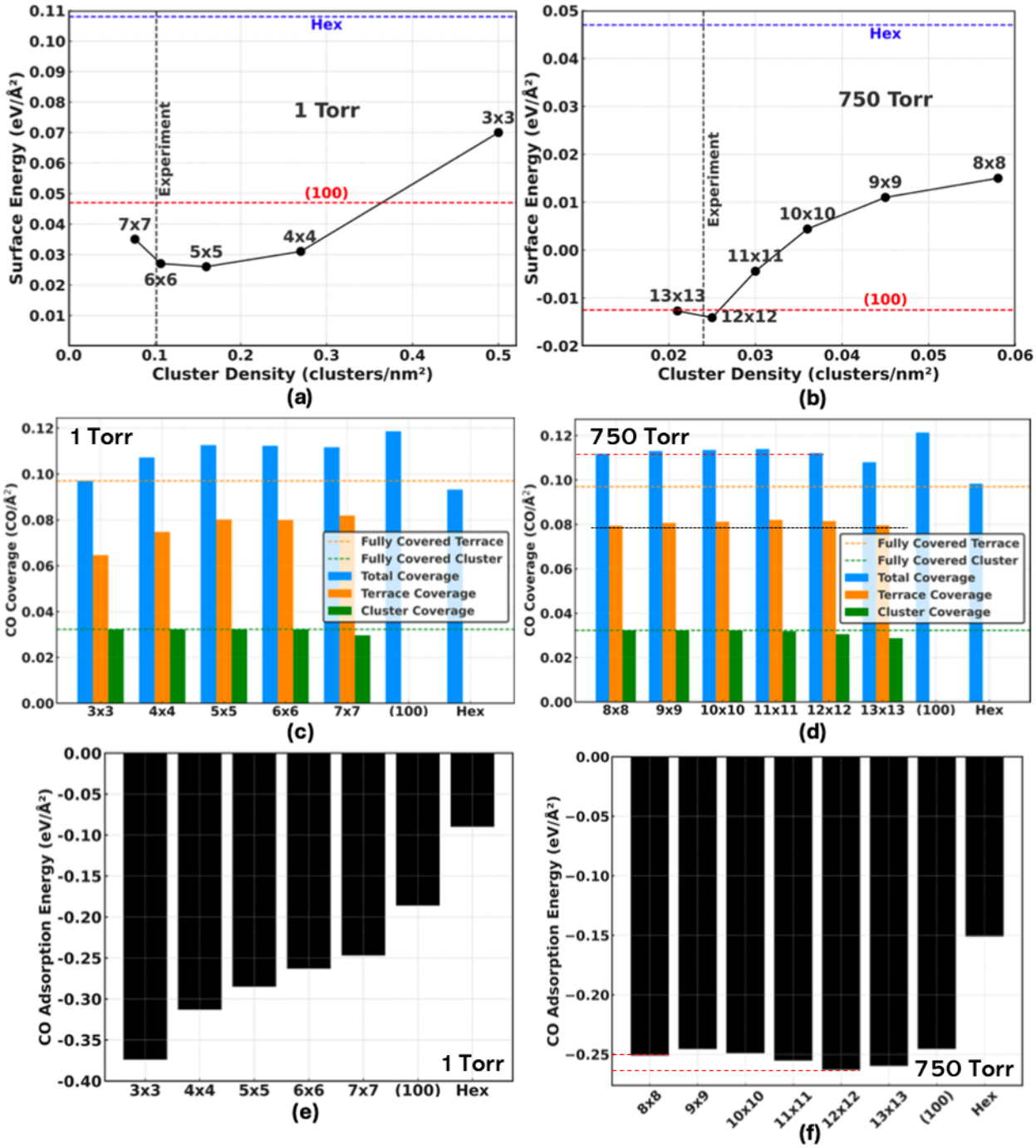

Figure 7. Calculated surface energies and CO coverages on (n×n) systems consisting of a n×n square Pt nanocluster on a 2n×2n unit cell of the Pt(100) surface for n=3-8 at 1 Torr and n=8-13 at 750 Torr. (a) Surface energies calculated with NNP for the (n×n) systems in a CO pressure of 1 Torr plotted as a function of the cluster density (number of nanoclusters per nm^2). For each system, the optimal CO coverage and arrangement is obtained by grand canonical basin hopping (GCBH) simulations. Surface energies of CO covered 1×1-Pt(100) and hex-Pt(100) are indicated by the horizontal red and blue dashed lines, respectively, while the cluster density for the considered CO pressure measured by HP-STM at 25°C is given by a vertical black dashed line. (b) Surface energies calculated with NNP for the (n×n) systems in a CO pressure of 750 Torr plotted as a function of the cluster density. (c, d) Calculated CO coverages (CO/Å^2) on the cluster (green), terrace (orange), and the total coverage (blue) for (c) (3×3) to (8×8)

nanoclusters under a CO pressure of 1 Torr at 25ºC plotted as a function of cluster density and (d) (8×8) to (13×13) nanoclusters under a CO pressure of 750 Torr at 25ºC plotted as a function of cluster density. Optimal CO coverages on pristine 1×1-Pt(100) and hex-Pt(100) surfaces are also given. For 1×1-Pt(100) and hex-Pt(100), total coverage and terrace coverage are identical as no cluster is present on either system. (e, f) Surface normalized CO adsorption energies for (e) (3×3) to (8×8) nanoclusters under CO pressure of 1 Torr and (f) (8×8) to (13×13) nanoclusters under CO pressure of 750 Torr.

Therefore, the optimum cluster size at thermodynamic equilibrium at 1 Torr CO, the 5×5 nanocluster, is slightly smaller than the optimum nanocluster size, the 6×6 cluster in CO at 2×10^{-8} Torr. This difference in the most stable structure aligns with the experimental finding where the cluster size decreases with increasing pressure in the range of 2×10^{-8} Torr to 1 Torr, as evidenced by the increase in cluster density observed by HP-STM in Figure 5d. One should however note that this change in optimal size is small and that the surface energy difference between the CO covered 5×5 and 6×6 clusters is also very small, about 1

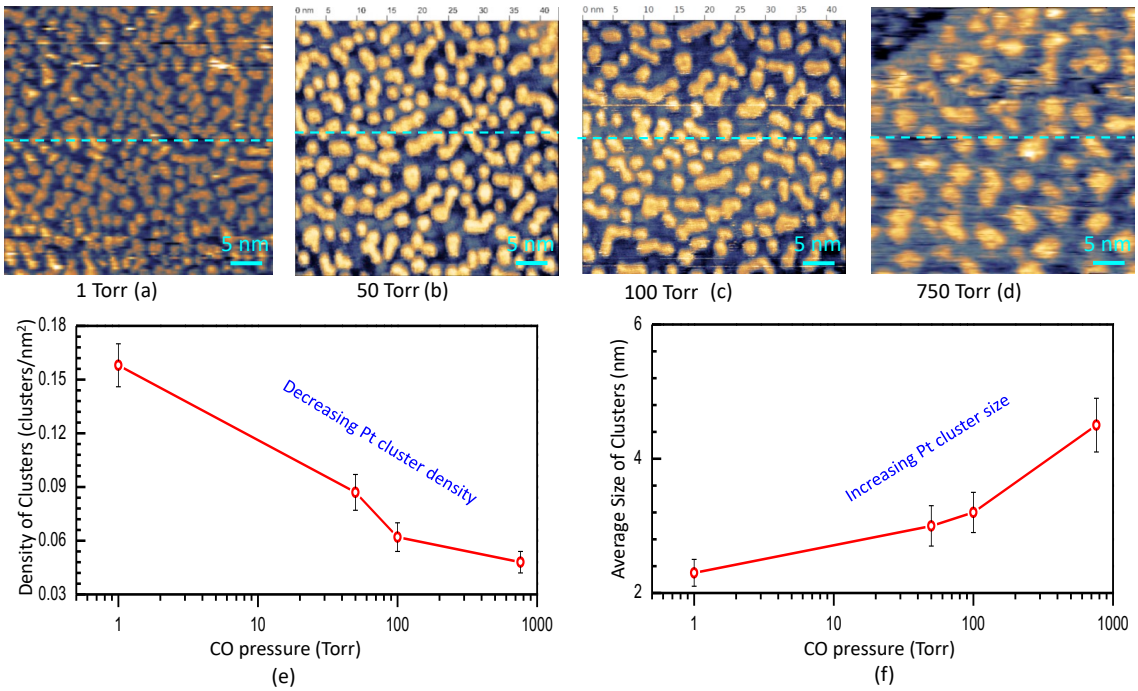

Figure 8. HP-STM images of Pt nanoclusters (area: 42 nm×42 nm) at 25ºC in CO gas at different pressures including 1 Torr, 50 Torr, 100 Torr, and 750 Torr and plots of density of nanoclusters and average size of nanoclusters at 25ºC as a function of CO pressure. (a) Image collected in CO at 1 Torr. (b) Image collected in CO at 50 Torr. (c) Image collected in CO at 100 Torr. (d) Image collected in CO at 750 Torr. (e) Plot of density of nanoclusters as a function of CO pressure. (f) Plot of average size of nanoclusters as a function of CO pressure.

meV/A^2, and hence might not be fully accurate with regard to the systematic error in DFT. In addition,

compared to the 6×6 cluster, the decrease in stability of the 7×7 cluster at 1 Torr in Figure 7a can be attributed to the 7×7 cluster being too large to sustain the full CO coverage of 1.0 on the cluster itself. This argument is supported by the lower CO coverage, 0.0304 CO/Å^2 on the 7×7 cluster (green bar marked with 7×7 in Figure 7c) than 0.0323 CO/Å^2 on the 6×6 cluster (green bar marked with 6×6 in Figure 7c). The cluster coverage continues to decrease at the 8×8 cluster size, falling to 0.0298 CO/Å^2. Figure S11d-e presents the optimized structures found through basin hopping using NNP for 6×6 and 7×7 nanoclusters at CO pressure of 1 Torr at 25ºC.

3.8 Significant coalescence of nanoclusters with an increase of CO pressure (1-750 Torr)

By using the same HP-STM, the structural evolution of Pt nanoclusters at 25ºC in the pressure range of 1-750 Torr was tracked. Figure 8a-d present STM images collected at 25ºC in CO at 1 Torr, 50 Torr, 100 Torr, and 750 Torr. Several images at each pressure were analyzed to calculate the average density of nanoclusters. Then, the nanocluster densities were plotted as a function of the corresponding CO pressure in Figure 8e. An intriguing observation is the significant decrease in nanocluster density with increasing CO pressure by a factor of about 4-5 in the considered pressure range (Figure 8e). This trend observed in the range of 1-750 Torr in Figure 8e aligns with the observed increase in the average size of nanoclusters with the increase of CO pressure in Figure 8f, since the number of Pt atoms of all nanoclusters, 25% of the Pt(100) surface, remain constant at different CO pressures.

Figure 9a, 9b, 9e, and 9f are atom-resolved images of the Pt nanoclusters and the terrace regions between them formed at 25ºC in 50 Torr CO. These high-resolution images allow us to check the arrangement of CO molecules adsorbed on nanoclusters and on the terrace. Images and line profile analyses in Figure 9a-d suggest the bright bumps on nanoclusters pack into a square lattice with a separation of 0.279 nm that is associated with a 100% CO coverage on Pt nanoclusters, as was the case for lower CO pressure. In addition, Figure 9e-h suggest that the adsorbed CO molecules on the terrace region between nanoclusters

pack into a dense layer, but not in a complete 1×1 pattern. This structure was previously assigned to a 8×2-14 CO overlayer corresponding to a coverage of 0.86 ML.[48]

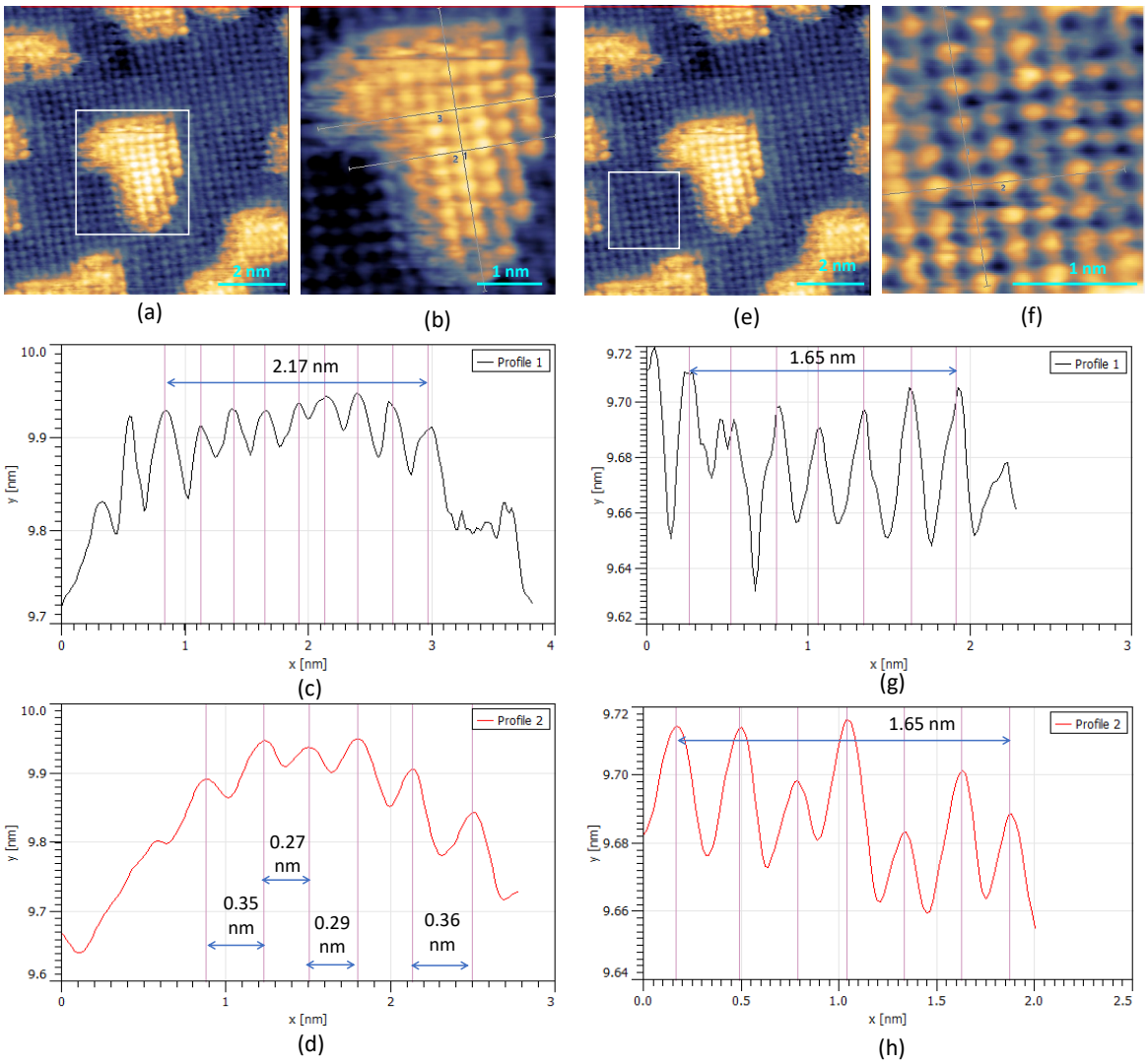

Figure 9. STM image of surface at 25°C in 50 Torr CO and line profile analysis for a nanocluster. (a) Image of surface collected at 25°C in 50 Torr of CO; 8.5 nm×8.5 nm. (b) Image of white rectangular area marked in (a); 3.9 nm×3.9 nm. (c) Line profile of line 1 in (b). (d) Line profile of line 2 in (b). (e) Image of surface collected at 25°C in 50 Torr of CO; 8.5 nm×8.5 nm. (f) Image of white rectangular area marked in (e); 2.1 nm×2.3 nm. Line profile analyses were conducted on the two lines 1 and 2. (g) Line profile of line 1. The average distance for the 6 inner CO molecules is 0.275 nm, very close the interatomic distance in a standard Pt(100) lattice. (h) Line profile of line 2; The average distance between these bumps is 0.28 nm.

3.9 Structural dynamics of nanoclusters at 25°C in CO at 100 Torr

The evolution of nanocluster density measured in the pressure range of 1-750 Torr CO clearly shows the formation of larger nanoclusters through coalescence in Figure 8e-f. Consistent with this statistical accounting, our in-situ tracking of the same area by HP-STM clearly catches the growth of nanoclusters at a timescale of 3-4 minutes. For instance, Figure 10a and 10b are two STM images sequentially collected from the same area consisting of tens of nanoclusters in 100 Torr CO with a time lapse of 3-4 minutes before Figure 8c was collected. Eight regions labelled R_1, R_2 ···R_8 in Figure 10a are marked with white ellipses. In each ellipse, 2-7 nanoclusters were enclosed and show clear growth over time of 3-4 minutes. Very clearly, small nanoclusters were merging into larger ones even at 25°C in 100 Torr CO.

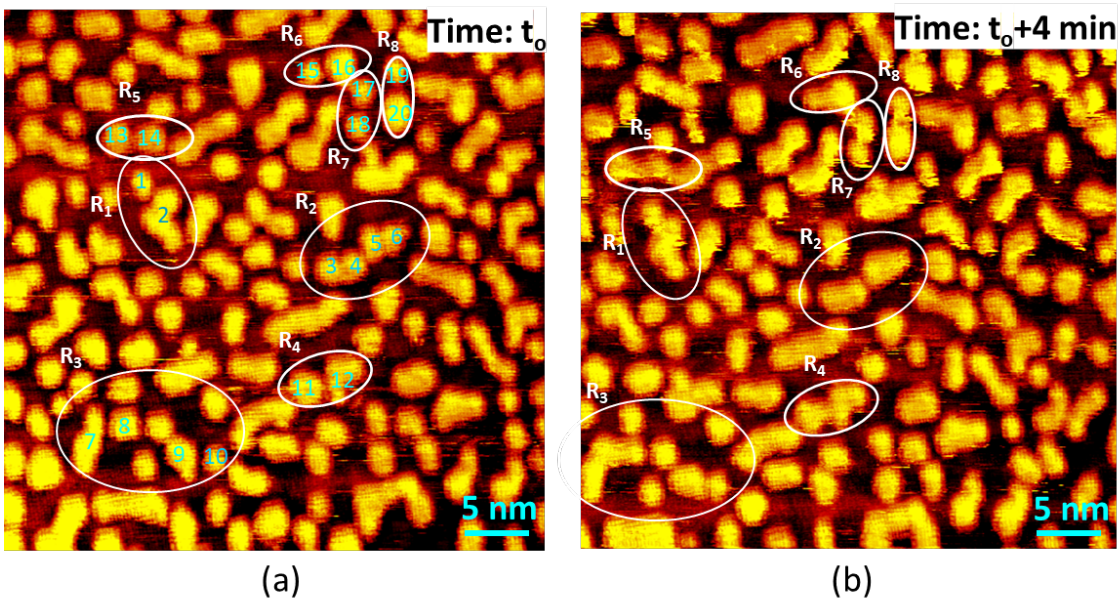

Figure 10. Two images collected from the same area of a sample surface at 25°C in 100 Torr CO with a time lapse of 3-4 minutes. Image *a* was collected before image *b*. Eight regions are marked as R_1-R_8 in images *a* and *b*. By comparing the same region such as R_6 in image *a* to R_6 in image *b*, coalescence of nanoclusters is readily confirmed.

3.10 Temperature-driven sintering of nanoclusters in CO at 750 Torr

As described in the introduction, CO is a reactant or product in many important reactions performed at elevated temperatures. Thus, it is crucial to explore how the surface of a metal nanoparticle catalyst in

CO responds to perturbation of reaction temperature. Two important questions are (1) whether the metal nanoclusters reach a thermodynamic equilibrium size upon increasing pressure of a reactant at room temperature and (2) whether the restructuring is kinetically limited. At low CO pressure range from 2×10^{-8} Torr to 1 Torr, the excellent agreement between the experimentally observed and theoretical nanocluster densities suggests that in the lower pressure regime at 25ºC, nanocluster structures approach their thermodynamic equilibrium state. However, surface evolution shifts from cluster nucleation and local rearrangement at lower pressure to major cluster coalescence at elevated pressure such as 750 Torr, thereby shifting the nature of the kinetic limitations on the system. For the purpose of addressing kinetic hindrance towards reaching equilibrium, we fixed the CO pressure at 750 Torr (1 bar) and increased the temperature of Pt nanoclusters from 25ºC in Figure 11a-b to 100ºC in Figure 11c-d and then to 130ºC (Figure 11e-f), followed by cooling from 130ºC in Figure 11g back to 25ºC (Figure 11h-i).

It is nearly impossible to use AP-XPS system to study structural evolution of these Pt nanoclusters in CO at 750 Torr. the collection of photoelectrons from a catalyst surface in a gas environment at 1 bar poses significant challenges for a lab-based Al Kα AP-XPS or a synchrotron-center AP-XPS using soft X-rays. On the other hand, while the membrane-sealed miniature cells have been developed and employed to study catalyst nanoparticles in 750 Torr gas phase,[64–70] they cannot study the surface of hex-Pt(100) at 25-130ºC in 750 Torr CO as it is impossible to perform high-temperature cleaning processes of the Pt single crystal at high temperature in a membrane-sealed miniature cell before a nanocluster model catalyst is prepared to explore temperate-dependent structural evolution. Thus, the HP-STM was the main technique to track the structural evolution of nanoclusters as a function of catalyst temperature in 750 Torr CO.

Figure 11j is the temperature map of this in-situ study of nanoclusters in 750 Torr CO using HP-STM. Our HP-STM effectively visualized the structural evolution and measured the density and average size of these nanoclusters in 750 Torr CO when annealing from 25ºC to 130ºC and then cooling from 130ºC to 25ºC, albeit with challenges in obtaining atom-resolved images due to the fast surface structure dynamics.

Images in Figure 11a-b, Figure 11c-d and Figure 11e-f were captured from nanoclusters on the same sample formed in 750 Torr CO at 25ºC, 750 Torr CO at 100ºC, and 750 Torr CO at 130ºC, respectively.

The nanocluster densities were measured from the images and then plotted as a function of temperature in Figure 11k. As the nanoclusters were heated from 25ºC to 100ºC in 750 Torr CO, the nanocluster density clearly decreased in Figure 11k, showing the sintering of Pt nanoclusters during the heating process. Statistical counting suggests that the density of Pt nanoclusters decreased by 50% at 100ºC compared to the initial density at 25ºC. This decrease in Pt nanocluster density when annealed from 25ºC to 100ºC is supported by the average size of nanoclusters at 100ºC, 7.5 nm (Figure 11c and 11d), compared to the average size of nanocluster at the initial 25ºC, 4.6 nm (Figure 11a and b). A green dashed line is marked in Figure 11a-d to help catch the increase of nanocluster size and decrease of nanocluster density from 25ºC in Figure 11a or b to 100ºC in Figure 11c or d.

The nanocluster density further decreased to 0.024 nanoclusters per nm^2 at 130ºC while annealed from 100ºC to 130ºC. These nanoclusters were then cooled from 130ºC to 25ºC in 750 Torr CO and HP-STM images were collected from this surface (Figures 11h and 11i). As shown in Figure 11k, the nanocluster densities at 25ºC (Figure 11h and 11i) upon cooling from 130ºC are nearly the same as those at 130ºC (Figures 11e-g). The preservation of nanocluster density upon cooling suggests that the nanoclusters initially formed at 25ºC (Figure 11a and b) were not at thermodynamic equilibrium but kinetically blocked at a smaller size. The kinetic limitation is relieved at a higher temperature in the range of 100-130ºC (Figure 11c-g) as the Pt nanoclusters now have sufficient energy to overcome the diffusion barrier of Pt atoms in the coalescence process, enabling these nanoclusters to reach their thermodynamic equilibrium size, 7.5 nm. This finding is significant since it justifies the significance of investigating nanocatalyst surface structures at catalysis temperature in a reactant gas.

3.11 Modelling Pt nanoclusters at 750 torr of CO

Since the average size of observed nanoclusters at equilibrium for a CO pressure of 750 Torr (7.5 nm) is larger than those observed from 2×10^{-8} Torr-1 Torr (2.8-2.3 nm), we used larger nanoclusters 8×8, 9×9, 10×10, 11×11, 12×12, and 13×13 in computational studies to simulate these systems formed at 750

Torr (Figure 7b). The energy stabilization trend previously discussed is maintained at high pressure. The 1×1-Pt(100) labelled with a red dashed line is markedly stabilized and now strongly competes with surfaces containing nanoclusters. Interestingly, the optimum size of these nanoclusters is much larger with the most stable size being a 12×12 Pt cluster in Figure 7b, corresponding to a cluster density of 0.025 clusters/nm². This result is based on thermodynamic analysis, and it agrees well with the experimentally measured cluster density at that pressure, *after* equilibration under CO pressure at 130ºC and cooling to 25ºC (0.023 clusters/nm^2) in Figure 11k. Therefore, our computational findings indicate that the size of the most stable nanocluster increases considerably with increasing CO pressure from 1 Torr (5×5 clusters) to 750 Torr (12×12 clusters), implying atom transport and surface restructuring, while the general mechanism of

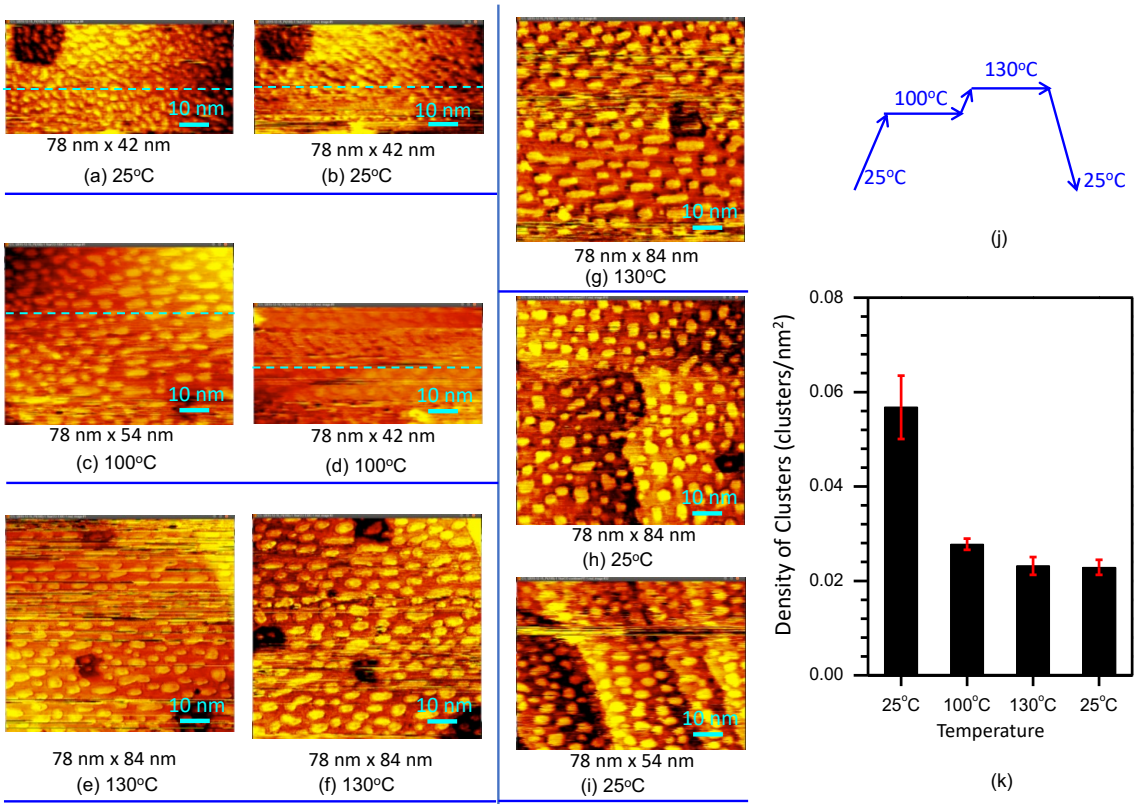

Figure 11. HP-STM images of Pt nanoclusters formed under a CO pressure of 750 Torr in the temperature range of 25-130ºC with a following cooling down to 25ºC. (a and b) Images collected at 25ºC in 750 Torr CO. (c and d) Images collected at 100ºC in 750 Torr CO. (e-g) Images collected at 130ºC in 750 Torr CO. (h and i) Images collected at 25ºC in 750 Torr CO after cooling from 130ºC in 750 Torr CO. (j) Plot of density of cluster as a function of temperature evolution in 750 Torr CO. The dashed lines in (a-d) can help to confirm the decrease of nanocluster density from (a-b) to (c-d) by accounting the number of nanoclusters on the dashed lines in (a or b) and (c or d) to find out the decrease of nanocluster density along increasing temperature from 25ºC to 100ºC.

nanocluster formation remains consistent over pressure. This corresponds to a decrease of the cluster density by a factor of ~6 from 0.16 clusters/nm^2 at 1 Torr (Figure 7a) to 0.025 clusters/nm^2 at 750 Torr (Figure 7b).

If we compare in further detail the surfaces containing 8×8 and 12×12 clusters (shown in Figures S12a and S13a, respectively) at the high CO pressure of 750 Torr, we see that the total CO coverage per unit surface area is very similar for the two cluster sizes (0.11 CO per Å^2, Figure 8d). The surface normalized free adsorption energy for CO is however slightly more negative for the 12x×2 (0.263 eV/Å^2) than for the 8×8 (0.251 eV/Å^2) as shown in Figure 7f.

As can be readily seen from the green bars in Figure 7d, the CO coverage on the nanocluster of the 12×12 system is lower than that on the 8×8 system. This is consistent with the incomplete occupancy of the 144 Pt atoms of the 12×12 nanocluster by 136 CO molecules (Figure S13a). However, we must consider the facts that (1) CO is adsorbing not only on the nanoclusters themselves but also on the terrace region between nanoclusters and (2) the area of the terrace region is about 3 times the total area of nanoclusters. Although the coverage of CO on the 12×12 nanocluster is lower than that on the 8×8 nanocluster, the CO coverage on the terrace region between 12×12 nanoclusters (orange bar for 12×12 in Figure 7d) is ~3% higher than on the terrace region between 8×8 nanoclusters (orange bar for 8×8 in Figure 7d). Consequently, the total CO coverage on the 12×12 system (blue bar for 12×12 system in Figure 7d) is similar to the 8×8 system (blue bar for 8×8 system in Figure 7d).

By calculating partial adsorption energies for CO molecules on the nanocluster and on the terrace, we see that the surface normalized nanocluster adsorption energy is more negative on the (8×8) system by 10% (owing to a higher cluster coverage and a higher fraction of Pt edges), while the surface normalized terrace adsorption energy is more negative on the 12×12 system by ~8%. By considering the normalized CO adsorption energies on both the cluster and the terrace, as well as the fact that the terrace is 3 times larger than the nanocluster in area, we found that the CO adsorption on the 12×12 system is more thermodynamically favorable than on the 8×8 system. The difference is, however, governed by the

adsorption on the terrace and not on the nanocluster itself. The influence of the cluster on the terrace stems from the fact that the fraction of the non-adsorption zone relative to the terrace is smaller on the 12×12 cluster compared to the 8×8 since the fraction of Pt-edge atoms on the 12×12 system is smaller than on the 8×8 system. Pt atoms of the terrace directly below the edge of the cluster present a high coordination with Pt, CN(Pt-Pt)=10 and thus cannot bind CO. A cluster of size n×n brings n^2 cluster sites but effectively blocks $(n+1)^2$ Pt atoms on the terrace. The unit cell for the n×n system has a size of 2n×2n and the number of Pt atoms accessible to CO, initially $4n^2$ on the pristine base, drops to $4n^2-(n+1)^2+n^2=4n^2-(2n+1)$ after placing the cluster. The relative number of lost sites $(2n+1)/4n^2$ is maximal for small clusters and decreases with size. A larger fraction of terrace sites is hence accessible to CO on the 12×12 cluster system, explaining the higher coverage and the more negative terrace adsorption energy in comparison to the 8×8 system. Therefore, the 12×12 nanocluster shows better stability at high CO pressure.

The optimum size of the Pt nanoclusters is determined by the competition between the clusters themselves, which prefer small sizes where CO adsorption energy is maximized, and the terrace regions between clusters, which prefer larger nanoclusters where the ratio of lost sites below the cluster edges is minimized. Thus, the optimum is the size at which full CO coverage (6×6 cluster at 2×10^{-8} Torr and 5×5 cluster at 1 Torr) or close to full CO coverage (12×12 cluster at 750 Torr) can be maintained on the nanocluster. As the coverage of CO on the nanocluster starts to significantly deviate from 1 ML, the stability of the system decreases. Going to a larger cluster size results in an important loss of adsorption energy on the nanocluster that generally cannot be compensated by the gain in CO adsorption energy on the terrace (except for the 12×12 cluster at 750 Torr).

4. Conclusions

Massive nanoclusters with size of 3.2±1.5 nm were prepared as a model catalyst of metal nanoparticles. We found that the density and average size of these Pt nanoclusters exhibit obvious pressure and temperature dependence. Although the nanocluster density in 1 Torr CO increases compared to 2×10^{-8} Torr CO, it remarkably decreases by a factor of 4-5 along with the increase of CO pressure from 1 to 750

Torr. The increase of nanocluster size at 25°C in 1-750 Torr is due to the competition between the stabilization effect of CO molecules adsorbed on the nanocluster edges and the destabilization effect of the non-adsorption zones around the nanocluster. Concurrent with the increase of CO pressure, the CO coverage on the terrace regions increases, decreasing surface energy and stabilizing the (n×n) systems. Compared to a n×n system comprised of small nanoclusters, the system consisting of relatively large nanoclusters benefits more from high CO pressure and exhibits lower surface energy. However, a system with nanoclusters that are too large experiences a decreased stabilization effect from the strong binding of CO on the edge Pt atoms since the fraction of the edge Pt atoms decreases with nanocluster size. Temperature-dependent structural evolution suggests that the structure of the nanoclusters formed at ambient pressure in reactant gas is not at equilibrium due to limited kinetics. Therefore, it does not represent the structure of nanoclusters at catalysis temperature under catalytic conditions. The kinetically hindered surface requires a slight annealing to a temperature range of 100-130°C to reach equilibrium size. The uncovered surface dynamics of Pt nanoclusters driven by CO pressures up to 750 Torr and temperatures up to 130°C demonstrate the dramatic structural transformations of metal nanoparticles at the atomic scale under reaction or catalytic conditions. The formation of Pt nanoclusters, followed by their pressure- and temperature-driven restructuring at 750 Torr CO, highlights the significance of imaging catalyst nanoparticle surfaces towards establishing an intrinsic correlation between the surface structure of metal nanoclusters and their catalytic activity. These insights gained from the integrated HP-STM and neural network potential-based computational studies strongly suggest that metal nanoparticle surfaces prepared under kinetic-controlled conditions, such as a relatively low synthesis temperature, may undergo substantial restructuring under elevated temperatures and do not represent the active phase of the metal catalysts in their initial, non-equilibrated state.

Supporting Information. Experimental procedures; Pt(100) preparation and characterization; high-pressure STM and AP-XPS methods; computational methods including DFT, neural network potential,

and grand canonical basin hopping; definitions of surface energy and CO coverage; additional STM images, structural models, and optimized nanocluster structures; validation of neural network potential; tables of surface energies, CO coverages, and adsorption energies.

Acknowledgements

The experimental part of this study (F. T. and L. N.) was supported by the Chemical Sciences, Geosciences and Biosciences Division, Office of Basic Energy Sciences, Office of Science, US Department of Energy under grant no. DE-SC0014561 and NSF-CHE-1800577. The theory part of this study (D. J. and P. S.) was funded by the National Science Foundation CDS&E grant 2152767. Computations in this work were performed on the Expanse Supercomputer and on the Bridges2 cluster through allocation CHE170060 from the Advanced Cyberinfrastructure Coordination Ecosystem: Services & Support (ACCESS) supported by the National Science Foundation.

References

(1) Cui, C.-H.; Li, H.-H.; Cong, H.-P.; Yu, S.-H.; Tao, F. (Feng). Direct Evidence for Active Site-Dependent Formic Acid Electro-Oxidation by Topmost-Surface Atomic Redistribution in a Ternary PtPdCu Electrocatalyst. *Chem. Commun.* **2012**, *48* (99), 12062. https://doi.org/10.1039/c2cc35822k.

(2) Li, J.; Tang, Y.; Ma, Y.; Zhang, Z.; Tao, F. (Feng); Qu, Y. In Situ Formation of Isolated Bimetallic PtCe Sites of Single-Dispersed Pt on CeO_2 for Low-Temperature CO Oxidation. *ACS Appl. Mater. Interfaces* **2018**, *10* (44), 38134–38140. https://doi.org/10.1021/acsami.8b15585.

(3) Bergman, S. L.; Granestrand, J.; Tang, Y.; París, R. S.; Nilsson, M.; Tao, F. F.; Tang, C.; Pennycook, S. J.; Pettersson, L. J.; Bernasek, S. L. In-Situ Characterization by Near-Ambient Pressure XPS of the Catalytically Active Phase of Pt/Al2O3 during NO and CO Oxidation. *Appl. Catal. B Environ.* **2018**, *220*, 506–511. https://doi.org/10.1016/j.apcatb.2017.08.047.

(4) Nguyen, L.; Zhang, S.; Yoon, S. J.; Tao, F. (Feng). Preferential Oxidation of CO in H_2 on Pure Co_3O_{4-x} and Pt/Co_3O_{4-x}. *ChemCatChem* **2015**, *7* (15), 2346–2353. https://doi.org/10.1002/cctc.201500320.

(5) Fung, V.; Hu, G.; Tao, F. (Feng); Jiang, D. Methane Chemisorption on Oxide-Supported Pt Single Atom. *ChemPhysChem* **2019**, *20* (17), 2217–2220. https://doi.org/10.1002/cphc.201900497.

(6) Tao, F.; Grass, M. E.; Zhang, Y.; Butcher, D. R.; Renzas, J. R.; Liu, Z.; Chung, J. Y.; Mun, B. S.; Salmeron, M.; Somorjai, G. A. Reaction-Driven Restructuring of Rh-Pd and Pt-Pd Core-Shell Nanoparticles. *Science* **2008**, *322* (5903), 932–934. https://doi.org/10.1126/science.1164170.

(7) Nguyen, L.; Zhang, S.; Wang, L.; Li, Y.; Yoshida, H.; Patlolla, A.; Takeda, S.; Frenkel, A. I.; Tao, F. (Feng). Reduction of Nitric Oxide with Hydrogen on Catalysts of Singly Dispersed Bimetallic Sites Pt_1Co_m and Pd_1Co_n. *ACS Catal.* **2016**, *6* (2), 840–850. https://doi.org/10.1021/acscatal.5b00842.

(8) Zeng, S.; Nguyen, L.; Cheng, F.; Liu, L.; Yu, Y.; Tao, F. (Feng). Surface Structure and Chemistry of Pt/Cu/Pt(1 1 1) near Surface Alloy Model Catalyst in CO. *Appl. Surf. Sci.* **2014**, *320*, 225–230. https://doi.org/10.1016/j.apsusc.2014.09.090.

(9) Nguyen, L.; Cheng, F.; Zhang, S.; Tao, F. (Feng). Visualization of Surfaces of Pt and Ni Model Catalysts in Reactive Environments Using Ambient Pressure High Temperature Scanning Tunneling Microscopy and Understanding the Restructurings of Surfaces of Model Metal Catalysts under Reaction Conditions at Near Ambient Pressure. *J. Phys. Chem. C* **2013**, *117* (2), 971–977. https://doi.org/10.1021/jp3086842.

(10) Zhang, S.; Shan, J.; Zhu, Y.; Frenkel, A. I.; Patlolla, A.; Huang, W.; Yoon, S. J.; Wang, L.; Yoshida, H.; Takeda, S.; Tao, F. (Feng). WGS Catalysis and In Situ Studies of CoO_{1-x}, $PtCo_n/Co_3O_4$, and $Pt_mCo_{m'}/CoO_{1-x}$ Nanorod Catalysts. *J. Am. Chem. Soc.* **2013**, *135* (22), 8283–8293. https://doi.org/10.1021/ja401967y.

(11) Karaca, H.; Safonova, O. V.; Chambrey, S.; Fongarland, P.; Roussel, P.; Griboval-Constant, A.; Lacroix, M.; Khodakov, A. Y. Structure and Catalytic Performance of Pt-Promoted Alumina-Supported Cobalt Catalysts under Realistic Conditions of Fischer–Tropsch Synthesis. *J. Catal.* **2011**, *277* (1), 14–26. https://doi.org/10.1016/j.jcat.2010.10.007.

(12) Yan, G.; Tang, Y.; Li, Y.; Li, Y.; Nguyen, L.; Sakata, T.; Higashi, K.; Tao, F. F.; Sautet, P. Reaction Product-Driven Restructuring and Assisted Stabilization of a Highly Dispersed Rh-on-Ceria Catalyst. *Nat. Catal.* **2022**, *5* (2), 119–127. https://doi.org/10.1038/s41929-022-00741-2.

(13) Li, B.; Kado, S.; Mukainakano, Y.; Miyazawa, T.; Miyao, T.; Naito, S.; Okumura, K.; Kunimori, K.; Tomishige, K. Surface Modification of Ni Catalysts with Trace Pt for Oxidative Steam Reforming of Methane. *J. Catal.* **2007**, *245* (1), 144–155. https://doi.org/10.1016/j.jcat.2006.10.004.

(14) Tao, F.; Salmeron, M. Surface Restructuring and Predictive Design of Heterogeneous Catalysts. *Science* **2024**, *386* (6724), eadq0102. https://doi.org/10.1126/science.adq0102.

(15) Tao, F. *Low-Temperature Activation and Catalytic Transformation of Methane to Non-CO_2 Products*; Wiley: Hoboken, 2025.

(16) García-Diéguez, M.; Pieta, I. S.; Herrera, M. C.; Larrubia, M. A.; Alemany, L. J. Nanostructured Pt- and Ni-Based Catalysts for CO2-Reforming of Methane. *J. Catal.* **2010**, *270* (1), 136–145. https://doi.org/10.1016/j.jcat.2009.12.010.
(17) Pantu, P.; Gavalas, G. R. Methane Partial Oxidation on Pt/CeO2 and Pt/Al2O3 Catalysts. *Appl. Catal. Gen.* **2002**, *223* (1–2), 253–260. https://doi.org/10.1016/S0926-860X(01)00761-X.
(18) Kim, S. S.; Lee, H. H.; Hong, S. C. A Study on the Effect of Support's Reducibility on the Reverse Water-Gas Shift Reaction over Pt Catalysts. *Appl. Catal. Gen.* **2012**, *423–424*, 100–107. https://doi.org/10.1016/j.apcata.2012.02.021.
(19) Anderson, R.; Griffin, K.; Johnston, P.; Alsters, P. L. Selective Oxidation of Alcohols to Carbonyl Compounds and Carboxylic Acids with Platinum Group Metal Catalysts. *Adv. Synth. Catal.* **2003**, *345* (4), 517–523. https://doi.org/10.1002/adsc.200390060.
(20) Wasserscheid, P.; Waffenschmidt, H. Ionic Liquids in Regioselective Platinum-Catalysed Hydroformylation. *J. Mol. Catal. Chem.* **2000**, *164* (1–2), 61–67. https://doi.org/10.1016/S1381-1169(00)00259-4.
(21) Zong, X.; Chu, Y.; Tang, Y.; Li, Y.; Wu, X.; Sun, Z.; Tao, F. Highly Selective Photocatalytic Synthesis of Acetic Acid at 0–25 °C. *Angew. Chem. Int. Ed.* **2024**, e202404598. https://doi.org/10.1002/anie.202404598.
(22) Gerhard Ertl; Helmut Knözinger; Ferdi Schüth; Jens Weitkamp. *Handbook of Heterogeneous Catalysis*, 2nd Edition.; Wiley-VCH: Weinheim, 2008.
(23) Gabor A. Somorjai. *Introduction to Surface Chemistry and Catalysis*, 2nd Edition.; Wiley: Hoboken, 2010.
(24) Howard F. Rase. *Handbook of Commercial Catalysts: Heterogeneous Catalysts*, 1st Edition.; CRC Press: Boca Raton, 2000.
(25) Salmeron, M.; Schlogl, R. Ambient Pressure Photoelectron Spectroscopy: A New Tool for Surface Science and Nanotechnology. *Surf. Sci. Rep.* **2008**, *63* (4), 169–199. https://doi.org/10.1016/j.surfrep.2008.01.001.
(26) Franklin Tao. *Application of Ambient Pressure X-Ray Photoelectron Spectroscopy to Catalysis*; John Wiley & Sons: Hoboken, 2023.
(27) Tao, F. (Feng). Design of an In-House Ambient Pressure AP-XPS Using a Bench-Top X-Ray Source and the Surface Chemistry of Ceria under Reaction Conditions. *Chem. Commun.* **2012**, *48* (32), 3812. https://doi.org/10.1039/c2cc17715c.
(28) Dou, J.; Sun, Z.; Opalade, A. A.; Wang, N.; Fu, W.; Tao, F. (Feng). Operando Chemistry of Catalyst Surfaces during Catalysis. *Chem. Soc. Rev.* **2017**, *46* (7), 2001–2027. https://doi.org/10.1039/C6CS00931J.
(29) (Feng) Tao, F.; Nguyen, L.; Zhang, S. Design of a New Reactor-like High Temperature near Ambient Pressure Scanning Tunneling Microscope for Catalysis Studies. *Rev. Sci. Instrum.* **2013**, *84* (3), 034101. https://doi.org/10.1063/1.4792673.
(30) Tao, F.; Tang, D.; Salmeron, M.; Somorjai, G. A. A New Scanning Tunneling Microscope Reactor Used for High-Pressure and High-Temperature Catalysis Studies. *Rev. Sci. Instrum.* **2008**, *79* (8), 084101. https://doi.org/10.1063/1.2960569.
(31) Nguyen, L.; Liu, L.; Assefa, S.; Wolverton, C.; Schneider, W. F.; Tao, F. F. Atomic-Scale Structural Evolution of Rh(110) during Catalysis. *ACS Catal.* **2017**, *7* (1), 664–674. https://doi.org/10.1021/acscatal.6b02006.
(32) Tao, F. (Feng); Crozier, P. A. Atomic-Scale Observations of Catalyst Structures under Reaction Conditions and during Catalysis. *Chem. Rev.* **2016**, *116* (6), 3487–3539. https://doi.org/10.1021/cr5002657.
(33) Zhang, D.; Virchenko, V.; Jansen, C.; Groot, I. M. N.; Juurlink, L. B. F. Adsorption Sites in the High-Coverage Limit of CO on Cu(111). *J. Phys. Chem. C* **2025**, *129* (7), 3493–3497. https://doi.org/10.1021/acs.jpcc.4c07044.

(34) Nazriq, N. K. M.; Krüger, P.; Yamada, T. K. Carbon Monoxide Stripe Motion Driven by Correlated Lateral Hopping in a 1.4 × 1.4 Monolayer Phase on Cu(111). *J. Phys. Chem. Lett.* **2020**, *11* (5), 1753–1761. https://doi.org/10.1021/acs.jpclett.9b03645.
(35) Yang, H. J.; Minato, T.; Kawai, M.; Kim, Y. STM Investigation of CO Ordering on Pt(111): From an Isolated Molecule to High-Coverage Superstructures. *J. Phys. Chem. C* **2013**, *117* (32), 16429–16437. https://doi.org/10.1021/jp404231t.
(36) Lin, Y.; Li, J.; Liang, X.; Hu, T.; Huang, Z.; Zhu, Z.; Diao, M.; Zhao, X.; Peng, Z.; Wang, Y.; Chen, Q.; Liu, J.; Wu, K. Steering Electron-Induced Surface Reaction via a Molecular Assembly Approach. *J. Am. Chem. Soc.* **2024**, *146* (14), 10150–10158. https://doi.org/10.1021/jacs.4c01623.
(37) Zhu, Y.; Xue, R.; Ren, H.; Chen, Y.; Yan, W.; Wu, B.; Duan, S.; Zhang, H.; Chi, L.; Xu, X. Reconstructing Pristine Molecular Orbitals from Scanning Tunneling Microscope Images via Artificial Intelligence Approaches. *JACS Au* **2025**, *5* (7), 3163–3170. https://doi.org/10.1021/jacsau.5c00310.
(38) Feng Tao; Miquel Salmeron; Gabor A. Somorjai. Scanning Tunneling Microscope Assembly, Reactor, and System. 8893309, November 18, 2014.
(39) Behler, J. Constructing High-dimensional Neural Network Potentials: A Tutorial Review. *Int. J. Quantum Chem.* **2015**, *115* (16), 1032–1050. https://doi.org/10.1002/qua.24890.
(40) Behler, J.; Parrinello, M. Generalized Neural-Network Representation of High-Dimensional Potential-Energy Surfaces. *Phys. Rev. Lett.* **2007**, *98* (14), 146401. https://doi.org/10.1103/PhysRevLett.98.146401.
(41) Kresse, G.; Hafner, J. *Ab Initio* Molecular Dynamics for Liquid Metals. *Phys. Rev. B* **1993**, *47* (1), 558–561. https://doi.org/10.1103/PhysRevB.47.558.
(42) Kresse, G.; Furthmüller, J. Efficiency of Ab-Initio Total Energy Calculations for Metals and Semiconductors Using a Plane-Wave Basis Set. *Comput. Mater. Sci.* **1996**, *6* (1), 15–50. https://doi.org/10.1016/0927-0256(96)00008-0.
(43) Perdew, J. P.; Burke, K.; Ernzerhof, M. Generalized Gradient Approximation Made Simple. *Phys. Rev. Lett.* **1996**, *77* (18), 3865–3868. https://doi.org/10.1103/PhysRevLett.77.3865.
(44) Singraber, A.; Morawietz, T.; Behler, J.; Dellago, C. Parallel Multistream Training of High-Dimensional Neural Network Potentials. *J. Chem. Theory Comput.* **2019**, *15* (5), 3075–3092. https://doi.org/10.1021/acs.jctc.8b01092.
(45) Singraber, A.; Behler, J.; Dellago, C. Library-Based *LAMMPS* Implementation of High-Dimensional Neural Network Potentials. *J. Chem. Theory Comput.* **2019**, *15* (3), 1827–1840. https://doi.org/10.1021/acs.jctc.8b00770.
(46) Sumaria, V.; Nguyen, L.; Tao, F. F.; Sautet, P. Atomic-Scale Mechanism of Platinum Catalyst Restructuring under a Pressure of Reactant Gas. *J. Am. Chem. Soc.* **2023**, *145* (1), 392–401. https://doi.org/10.1021/jacs.2c10179.
(47) Sumaria, V.; Sautet, P. CO Organization at Ambient Pressure on Stepped Pt Surfaces: First Principles Modeling Accelerated by Neural Networks. *Chem. Sci.* **2021**, *12* (47), 15543–15555. https://doi.org/10.1039/D1SC03827C.
(48) Sumaria, V.; Nguyen, L.; Tao, F. F.; Sautet, P. Optimal Packing of CO at a High Coverage on Pt(100) and Pt(111) Surfaces. *ACS Catal.* **2020**, *10* (16), 9533–9544. https://doi.org/10.1021/acscatal.0c01971.
(49) Ritter, E.; Behm, R.; PfiTSCHKE, G.; Winttern, J. DIRECT OBSERVATION OF A NUCLEATION AND GROWTH PROCESS ON AN ATOMIC SCALE.
(50) Fiorentini, V.; Methfessel, M.; Scheffler, M. Reconstruction Mechanism of Fcc Transition Metal (001) Surfaces. *Phys. Rev. Lett.* **1993**, *71* (7), 1051–1054. https://doi.org/10.1103/PhysRevLett.71.1051.
(51) Deskins, N. A.; Lauterbach, J.; Thomson, K. T. Lifting the Pt{100} Surface Reconstruction through Oxygen Adsorption: A Density Functional Theory Analysis. *J. Chem. Phys.* **2005**, *122* (18), 184709. https://doi.org/10.1063/1.1893718.

(52) Gardner, P.; Martin, R.; Tüshaus, M.; Bradshaw, A. M. The Adsorbate-Induced Lifting of the Pt100 Surface Reconstruction: IRAS Investigations. *J. Electron Spectrosc. Relat. Phenom.* **1990**, *54–55*, 619–628. https://doi.org/10.1016/0368-2048(90)80254-8.
(53) Kim, M.; Sim, W. S.; King, D. A. CO-Induced Removal of the Pt{100}-Hex Reconstruction Studied by RAIRS. *J. Chem. Soc. Faraday Trans.* **1996**, *92* (23), 4781. https://doi.org/10.1039/ft9969204781.
(54) Tao, F.; Dag, S.; Wang, L.-W.; Liu, Z.; Butcher, D. R.; Salmeron, M.; Somorjai, G. A. Restructuring of Hex-Pt(100) under CO Gas Environments: Formation of 2-D Nanoclusters. *Nano Lett.* **2009**, *9* (5), 2167–2171. https://doi.org/10.1021/nl900809u.
(55) Van Beurden, P.; Bunnik, B. S.; Kramer, G. J.; Borg, A. Mechanism and Dynamics of the CO-Induced Lifting of the Pt(100) Surface Reconstruction. *Phys. Rev. Lett.* **2003**, *90* (6), 066106. https://doi.org/10.1103/PhysRevLett.90.066106.
(56) Hove, M. A. V.; Koestner, R. J.; Kesmodel, L. L. THE SURFACE RECONSTRUCTIONS OF THE (100) CRYSTAL FACES OF IRIDIUM, PLATINUM AND GOLD.
(57) Ritz, G.; Schmid, M.; Varga, P.; Borg, A.; Rønning, M. Pt(100) Quasihexagonal Reconstruction: A Comparison between Scanning Tunneling Microscopy Data and Effective Medium Theory Simulation Calculations. *Phys. Rev. B* **1997**, *56* (16), 10518–10525. https://doi.org/10.1103/PhysRevB.56.10518.
(58) Helms, C. R.; Bonzel, H. P.; Kelemen, S. The Effect of the Surface Structure of Pt on Its Electronic Properties and the Adsorption of CO, O2, and H2: A Comparison of Pt(100) – (5×20) and Pt(100) – (1×1). *J. Chem. Phys.* **1976**, *65* (5), 1773–1782. https://doi.org/10.1063/1.433323.
(59) Norton, P. R.; Davies, J. A.; Creber, D. K.; Sitter, C. W. THE Pt(100) (5 X 20) = (1 X 1) PHASE T~NSITION: A STUDY BY RUTHERFORD BACKSCATTERING, NUCLEAR MICROANALYSIS, LEED AND TH~~AL DESO~TI~N SPECTROSCOPY.
(60) Davies, J. A.; Norton, P. R. ABSOLUTE COVERAGE MEASUREMENT OF ADSORBED CO AND Dz ON PLATINUM.
(61) Amann, P.; Degerman, D.; Lee, M.-T.; Alexander, J. D.; Shipilin, M.; Wang, H.-Y.; Cavalca, F.; Weston, M.; Gladh, J.; Blom, M.; Björkhage, M.; Löfgren, P.; Schlueter, C.; Loemker, P.; Ederer, K.; Drube, W.; Noei, H.; Zehetner, J.; Wentzel, H.; Åhlund, J.; Nilsson, A. A High-Pressure x-Ray Photoelectron Spectroscopy Instrument for Studies of Industrially Relevant Catalytic Reactions at Pressures of Several Bars. *Rev. Sci. Instrum.* **2019**, *90* (10), 103102. https://doi.org/10.1063/1.5109321.
(62) Tao, F. F.; Nguyen, L.; Zhang, S.; Li, Y.; Tang, Y.; Zhang, L.; Frenkel, A. I.; Xia, Y.; Salmeron, M. Formation of Second-Generation Nanoclusters on Metal Nanoparticles Driven by Reactant Gases. *Nano Lett.* **2016**, *16* (8), 5001–5009. https://doi.org/10.1021/acs.nanolett.6b01718.
(63) Tao, F.; Dag, S.; Wang, L.-W.; Liu, Z.; Butcher, D. R.; Bluhm, H.; Salmeron, M.; Somorjai, G. A. Break-Up of Stepped Platinum Catalyst Surfaces by High CO Coverage. *Science* **2010**, *327* (5967), 850–853. https://doi.org/10.1126/science.1182122.
(64) Tao, F.; Nguyen, L.; Amati, M.; Gregoratti, L. Preparation of a Membrane-Sealed Cell for Studying Catalyst Nanoparticles in Flowing Gas with High Vacuum x-Ray Photoelectron Spectrometer. *Rev. Sci. Instrum.* **2024**, *95* (5), 055108. https://doi.org/10.1063/5.0186088.
(65) Wu, C. H.; Weatherup, R. S.; Salmeron, M. B. Probing Electrode/Electrolyte Interfaces in Situ by X-Ray Spectroscopies: Old Methods, New Tricks. *Phys. Chem. Chem. Phys.* **2015**, *17* (45), 30229–30239. https://doi.org/10.1039/C5CP04058B.
(66) Velasco-Velez, J. J.; Pfeifer, V.; Hävecker, M.; Weatherup, R. S.; Arrigo, R.; Chuang, C.; Stotz, E.; Weinberg, G.; Salmeron, M.; Schlögl, R.; Knop-Gericke, A. Photoelectron Spectroscopy at the Graphene–Liquid Interface Reveals the Electronic Structure of an Electrodeposited Cobalt/Graphene Electrocatalyst. *Angew. Chem. Int. Ed.* **2015**, *54* (48), 14554–14558. https://doi.org/10.1002/anie.201506044.

(67) Weatherup, R. S.; Eren, B.; Hao, Y.; Bluhm, H.; Salmeron, M. B. Graphene Membranes for Atmospheric Pressure Photoelectron Spectroscopy. *J. Phys. Chem. Lett.* **2016**, *7* (9), 1622–1627. https://doi.org/10.1021/acs.jpclett.6b00640.
(68) Velasco-Vélez, J. J.; Pfeifer, V.; Hävecker, M.; Wang, R.; Centeno, A.; Zurutuza, A.; Algara-Siller, G.; Stotz, E.; Skorupska, K.; Teschner, D.; Kube, P.; Braeuninger-Weimer, P.; Hofmann, S.; Schlögl, R.; Knop-Gericke, A. Atmospheric Pressure X-Ray Photoelectron Spectroscopy Apparatus: Bridging the Pressure Gap. *Rev. Sci. Instrum.* **2016**, *87* (5), 053121. https://doi.org/10.1063/1.4951724.
(69) Nguyen, L.; Tao, P. P.; Liu, H.; Al-Hada, M.; Amati, M.; Sezen, H.; Gregoratti, L.; Tang, Y.; House, S. D.; Tao, F. F. X-Ray Photoelectron Spectroscopy Studies of Nanoparticles Dispersed in Static Liquid. *Langmuir* **2018**, *34* (33), 9606–9616. https://doi.org/10.1021/acs.langmuir.8b00806.
(70) Nguyen, L.; Tao, P. (Pengcheng); Liu, H.; Al-Hada, M.; Amati, M.; Sezen, H.; Tang, Y.; Gregoratti, L.; Tao, F. (Feng). Studies of Surface of Metal Nanoparticles in a Flowing Liquid with XPS. *Chem. Commun.* **2018**, *54* (71), 9981–9984. https://doi.org/10.1039/C8CC03497D.

TOC graphic

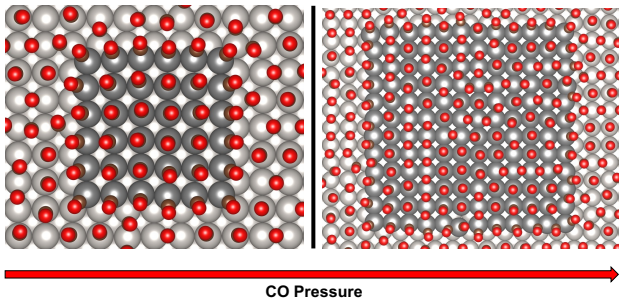

.